Electron Backscatter Diffraction beyond the mainstream

Gert Nolze*[,1], Ralf Hielscher[2], Aimo Winkelmann[3]

[1] Federal Institute for Materials Research and Testing (BAM), Berlin, Germany
[2] Faculty of Mathematics, TU Chemnitz, Germany
[3] Bruker Nano GmbH, Berlin, Germany

Received XXXX, revised XXXX, accepted XXXX
Published online XXXX

Key words: element number contrast, channeling-in and out, pseudosymmetry, polarity, lattice parameters.

* Corresponding author: e-mail gert.nolze@bam.de, Phone: +49-30-8104 3513, Fax: +49-30-8104 1517

We present special applications of electron backscatter diffraction (EBSD) which aim to overcome some of the limitations of this technique as it is currently applied in the scanning electron microscope. We stress that the raw EBSD signal carries additional information which is useful beyond the conventional orientation determination. The background signal underlying the backscattered Kikuchi diffraction (BKD) patterns reflects the chemical composition and surface topography but also contains channeling-in information which is used for qualitative real-time orientation imaging using various backscattered electron signals. A significantly improved orientation precision can be achieved when dynamically simulated pattern are matched to the experimental BKD patterns. The breaking of Friedel's rule makes it possible to obtain orientation mappings with respect to the point-group symmetries. Finally, we discuss the determination of lattice parameters from individual BKD patterns.

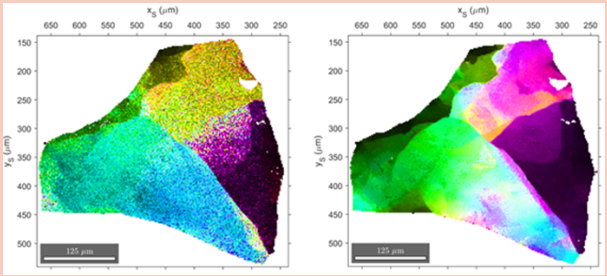

Subgrain structure in a single quartz grain. The increased noise level in the left map reflects the lower precision of a standard orientation determination using band detection by the Hough transform. The right map results from the same experimental raw data after orientation refinement using a pattern matching approach. The colors correspond an adapted inverse pole figure color key with a maximum angular deviation of about 2° from the mean orientation.

1 Introduction Electron backscatter diffraction (EBSD) in the scanning electron microscope (SEM) allows a comprehensive characterization of crystalline materials, especially when combined with chemically sensitive techniques like energy dispersive x-ray spectroscopy (EDX). The range of materials to which EBSD can be applied is very broad as long as the respective phases are sufficiently crystalline, stable in vacuum, withstand an intense bombardment with electrons, and do not charge significantly. As an extreme example, even quasicrystals form high-qualitative diffraction patterns as seen in Fig. 1 (see also [1]).

2 Experimental

2.1 Setup All measurements have been performed using a LEO 1530VP (ZEISS) scanning electron microscope (SEM) with a field-emission gun. The SEM was equipped with a Bruker EBSD and EDX system. The EBSD detector e^-Flash^{HR+} uses a camera with a maximum resolution of 1600×1200 pixels, and for the investigations shown here, the images were usually binned to a final size of 160×115 pixels[1] and stored for a further post-processing. The built-in camera has a maximal gray-scale

[1] this includes 4% clipping of the pattern at the top due to hardware restrictions

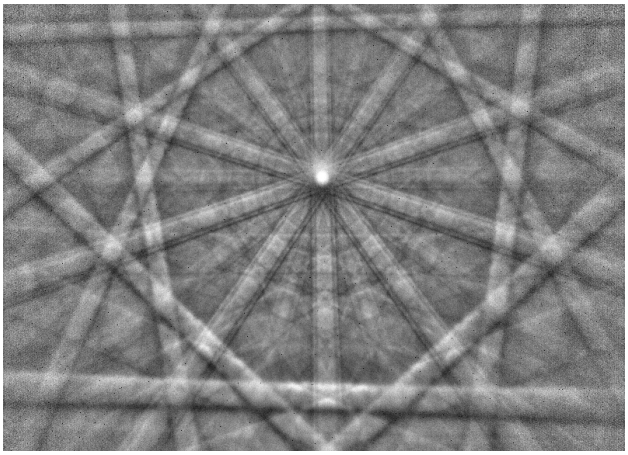

Figure 1 Backscattered Kikuchi diffraction of a quasicrystal reflecting the decagonal rotation symmetry around [0 0 0 0 1].

sensitivity of 12 bits but has been operated in 8-bit mode. Conventional EBSD and EDX data analysis was done with ESPRIT 1.9 (Bruker Nano).

Adjacent to the detecting phosphor screen, five semiconductor diodes are mounted for real-time sample imaging, cf. Fig. 2 (a). These diodes deliver four different backscattered electron (BSE) signals which can be individually mixed and displayed as a gray-scale or color images (ARGUS™, Bruker Nano).

2.2 Sample preparation All samples have been manually prepared using standard procedures. Starting with a typical metallographic preparation (grinding with coated abrasive grinding papers down to 1200SiC and polishing with diamond 3 µm and 1µm) the surface preparation has been finished by polishing with colloidal silica. The final polishing time varies with the material but was always in the range of a few minutes only (Mastermed 2 (Buehler) 10-15 min and OPS (Struers) 5 min).

2.3 Acquisition conditions The acquisition conditions for the presented examples are listed in Table 1. Acquisition conditions differ from material to material. Sometimes also an acquisition in low vacuum was necessary in order to prevent a detrimental drift at higher magnifications. Since the quality of the primarily used diffraction signal depends on several factors like the acceleration voltage, the beam current, the diffracting phase, and the defect concentration, a frame averaging has been applied when the signal-to-noise ratio appeared to be too low for the specific investigation. Nevertheless, we tried to use standard acquisition conditions in order to test the general practicability of the applied procedures. Systematic investigations by variation of single parameters like number of frames have not been performed explicitly, i.e., the shown results can be easily improved by a specific optimization of the acquisition conditions. For imaging as well as EBSD investigations always a sample-screen distance of 18 mm has been used. In all results shown, no data cleaning procedures have been applied.

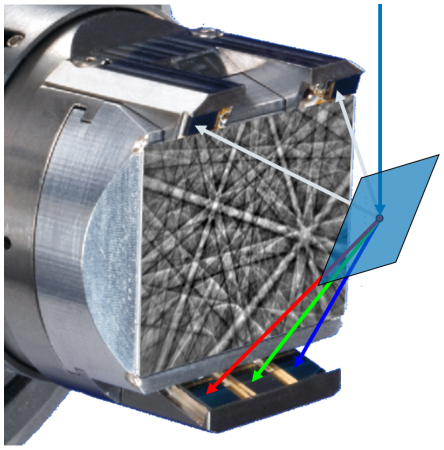

a) BSE detector positions (ARGUS™, Bruker Nano)

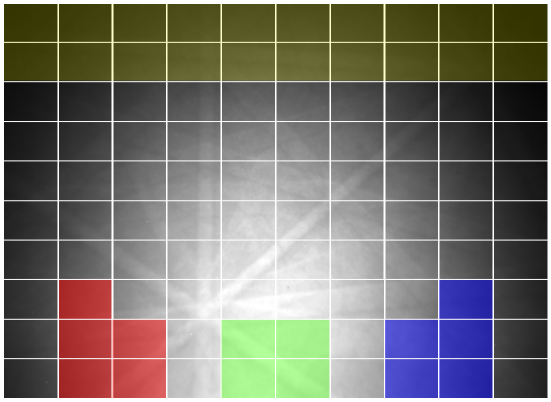

b) raw EBSD signal subdivided for post-processing

Figure 2 Comparison between the direct detection of BSE using several detectors mounted around the phosphor screen (a), and the use of the raw EBSD signal defining specific regions as detecting areas (b). The yellow-colored part at the top and the upper diodes are suitable for imaging of chemical composition whereas the red, green and blue regions at the bottom and the lower diodes are preferred to image orientation contrast.

2.4 Kikuchi Pattern Simulations The diffraction pattern simulation used here is based on the dynamical theory of electron diffraction [2]. The software ESPRIT DynamicS (Bruker Nano) provides an automatic pattern matching of simulated and experimental diffraction patterns based on the optimization of the cross-correlation coefficient between two images. The normalized cross-correlation coefficient r is defined as [3,4]:

$$r = \frac{\sum_{i,j} \left[f(i,j) - \bar{f} \right] \cdot \left[w(i,j) - \bar{w} \right]}{\sqrt{\sum_{i,j} \left[f(i,j) - \bar{f} \right]^2} \cdot \sqrt{\sum_{i,j} \left[w(i,j) - \bar{w} \right]^2}}. \quad (1)$$

Table 1 Measurement conditions during EBSD mapping performed at $E_o = 20$ kV. All raw patterns were stored with a size of 160×115 pixels. The EBSD system uses per default a Hough resolution of 60 in r (distance)and ϕ (slope) applied on an invariable pattern size of only 80x57 pixels. The number in parentheses behind the sample refers to the respective figure number.

Sample	beam current [nA]	chamber pressure [Pa]	step size [µm]	dwell time [ms]	No frames
rock (4)	7	13	4.840	20	3
CMSX (5)	11	–	0.042	9	1
FeO (6)	7	13	0.150	30	1
SiO_2 (10)	7	11	1.990	16	3
FeS_2 (15)	7	7	0.060	25	2
GaN (17)	11	10	0.096	24	1
ZnO (18)	11	–	0.170	12	4
Co-Al (20)	8	–	0.056	17	1

where $f(i,j)$ and $w(i,j)$ are the pixel intensity values of the corresponding regions of interest (ROI) in the two patterns to be compared, while $\bar{f}$ and $\bar{w}$ are the mean values in these ROIs. The absolute value of r is in the range between 0 and 1 and does not depend on scale changes in the intensity of both patterns. From our experience, values of $r > 0.6...0.7$ indicate visually convincing fits between experimental and simulated values. For pattern matching or model discrimination via r, the statistically necessary levels of r could be lower or higher than these values, depending on the details of the application. For imaging applications, we also apply the cross-correlation coefficient to analyze the similarity of experimental patterns within a mapped sample region, see Figure 20. The simulations presented here neglect experimental excess-deficiency effects which are related to the incident beam direction [5].

3 Imaging by using the EBSD signal It is well known that angle-resolved detection of electrons in specific energy ranges can provide useful imaging modalities in the SEM [6–8]. Imaging in the SEM uses specific detectors which collect various signals, including electrons after interaction with the sample, locally generated x-rays, or even emitted light.

For high energy BSE often semiconductor detectors are used [9]. In case of highly tilted surfaces, imaging with horizontally aligned standard BSE detectors is not very efficient anymore, and also the detection of secondary electrons is extremely restricted because of the close distance between sample and EBSD detector. Like seen in Fig. 2 (a), many EBSD detectors can be equipped with detector diodes placed around the phosphor screen, providing orientation and phase contrast in the SEM [10–14].

3.1 Data content of EBSD Patterns The backscattered electrons show of a wide range of energies and originate from an extended depth range. Without any reference to the physical meaning, it is useful to regard the measured raw EBSD signal as a superposition of a Kikuchi diffraction (KD) pattern containing the actual diffraction modulation and a smooth background intensity (BG). This purely empirical interpretation is based on the image processing that is usually applied to the raw data to effectively extract the diffraction modulation KD = EBSD - BG for crystallographic analysis. We refer to the raw 2D signal measured by the camera in the EBSD detector hardware as the "EBSD pattern". In the conventional EBSD in backscattering geometry, we call the KD pattern a backscattered Kikuchi diffraction (BKD) pattern, while in transmission mode t-EBSD we have a transmission Kikuchi diffraction (TKD) pattern.

Especially the anisotropic intensity distribution of the background shown in Fig. 2 (b) strongly depends on the sample tilt, the electron energy and the interacting material, see for example [9,15]. But also the BKD pattern reflects asymmetric excess-deficiency effects which result from the flat angle of the electron beam entering the sample surface, cf. Fig. 2 (a).

When using a phosphor screen, the visible EBSD signal is not formed by BSEs of lower energy since their energy is too small to produce light in the phosphor, effectively resulting to some energy filtering of the BSEs.

The post-processing of the EBSD signal is based on the assumption that the essential part of the modulation is caused by diffraction. Therefore, for the crystallographic interpretation the modulated part is most relevant. The usefulness of the raw signal with the dominating background intensity has been pointed out as a possible replacement for an absent hardware BSE detector [16]. We note that the general physical formation process of the EBSD pattern usually cannot be divided into physical processes for the KD and the BG fractions separately, but both fractions instead contain contributions from the combined action of multiple elastic and inelastic scattering processes in a more or less imperfect crystal where the coherence of the scattered electron waves can be affected in various different ways. Specifically, it can be very misleading to draw physical conclusions based solely on the empirical partition of EBSD = KD + BG, which is most prominently seen by the fact that diffraction processes also result in the formation of a "background intensity" [17]. Thus, the background signal is *not* "formed by electrons which are not diffracted" and the background signal *also* contains electrons which have been quasi-elastically scattered. From a different point of view, this illustrates the ambiguity of the assignment of KD and BG in an actual experimental pattern. To be absolutely reproducible, the image processing procedure to obtain KD and BG would have to be exactly stated.

3.2 The detector screen as an imaging tool From Fig 2(a) it becomes clear that, compared to the phosphor screen, the size of the BSE diodes is relatively small. Moreover, their position outside the main intensity maximum as well as the limited solid angle limit their imaging capabil-

ities further. Since the same BSE signal that is incident on the semiconductor diodes also produces a large number of light quanta on the phosphor screen, several studies used the phosphor screen as a 2D BSE detector [16, 18–20, 14, 21]. In contrast to the mounted detector diodes, position, size, number and signal combination of virtual detectors can be freely defined as regions of interest (ROI) on the EBSD pattern. This flexibility offers a wide range of applications [14].

Backscattered electrons are sensitive to different types of information, namely

a) the mean atomic number $\bar{Z}$ of a phase,
b) the surface topography, and
c) the crystal orientation [22].

ROIs which are sensitive with respect to $\bar{Z}$ (yellow at the top) or the crystal orientation (red, green and blue at the bottom) are exemplarily highlighted in Fig. 2 (b) by different colors.

It is unfortunate that the different signal components are superimposed in the final signal. The relative impact of each signal component depends on the phase-specific mix of chemistry, the crystal and surface-near inherent defect structure (channeling in and out), and the sample preparation (induced defect structure and surface topography as result of the phase resistance against the preparation technique applied). This mix makes any unequivocal interpretation of BSE images in general difficult. However, via a suitable definition and combination of virtual detector areas on the detector region, often even a semi-quantitative interpretation can be very helpful.

3.3 Atomic number contrast The top region of the EBSD screen represents a sector which is nearly vertical to the sample surface, see Fig. 2 (a). This sector can be sensitive to the chemical composition of a phase [19, 20, 14], with the accumulated intensity being in first approximation proportional to the backscattered coefficient η.

For the prediction of η, several non-linear fits have been proposed. A short compilation is given in [23]. Some of them try to find a physically reasonable equation based on the mean atomic number $\bar{Z}$, other simply refine experimental data by matching a polynomial as function of $\bar{Z}$. Because of the better match for high as well as low $\bar{Z}$ we prefer an often used polynomial described e.g. in [9]:

$$\eta = -0.0254 + 0.016\bar{Z} - 1.186\times10^{-4}\bar{Z}^2 + 8.3\times10^{-7}\bar{Z}^3. \quad (2)$$

A challenging term is also $\bar{Z}$ which is differently defined in literature. We are using

$$\bar{Z} = \sum_{i=1}^{n} c_i Z_i. \quad (3)$$

c_i describes the concentration of atom i with atomic number Z_i. More about the different approaches, their benefits and limitations are discussed for example in [24–27]. The curve of the polynomial is shown in Fig. 3.

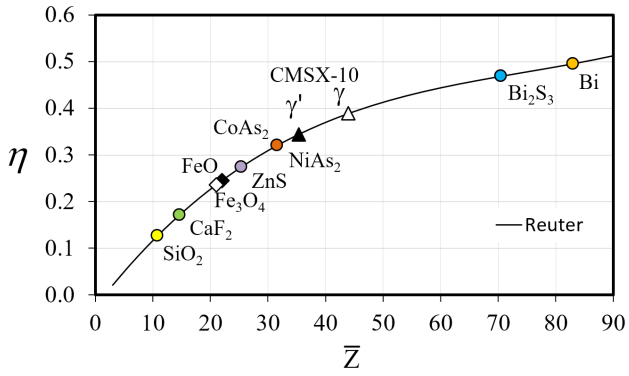

Figure 3 The backscatter coefficient η as function of the mean atomic number $\bar{Z}$, cf. equ. (2). The microstructure in Fig. 4 contains phases which cover nearly the entire $\bar{Z}$ range. In this case, the gray-scale resolution is too low to distinguish between phases of small $\Delta\bar{Z}$.
Additionally, γ and γ' of CMSX-10 as well as FeO and Fe_3O_4 are given.

It is clear that η does not have the energy resolution of EDX, however, in contrast to EDX it reflects the impact of *all* material constituents, i.e., also light elements which are invisible for EDX detectors. Examples are given in [26–30]. Moreover, the BSE signal has a higher spatial resolution than EDX. Therefore, compared to an element distribution map collected by EDX, BSE images can have remarkable advantages for phase differentiation. Furthermore, a from EBSD pattern derived η map neither requires an EDX signal nor a BSE detector [31]. This is beneficial when the acquisition conditions like dwell time or working distance of EBSD and EDX are incompatible. The only requirement is that all raw EBSD patterns, i.e., including the background, have been stored so that they can be reprocessed again.

3.3.1 Significant differences in $\bar{Z}$ Phase discrimination and phase identification by EBSD is limited, which is especially pronounced in the case of cubic phases. Unfortunately, there are practically no tools available which indicate to the user that an EBSD analysis is likely to run into problems. Patterns can be well indexed for an incorrectly selected phase, databases are full of similar entries, or the acquired EBSD pattern and EDX signal do not match to any phase. Major relevant influences in the EBSD pattern are pseudosymmetry and the comparatively low sensitivity regarding lattice parameter variations. Therefore, all the more important is that the available information like the BSE intensity can be used to confirm or increase the confidence of the selected phase candidates. This becomes essential when the EDX signal cannot be used as a discriminator, e.g. in case of structures of sizes below the resolution of EDX, or if low-atomic mass elements like H or Li cannot be ruled out.

An example of the direct use of the raw EBSD signal on the screen is given in Fig. 4, which shows derived images

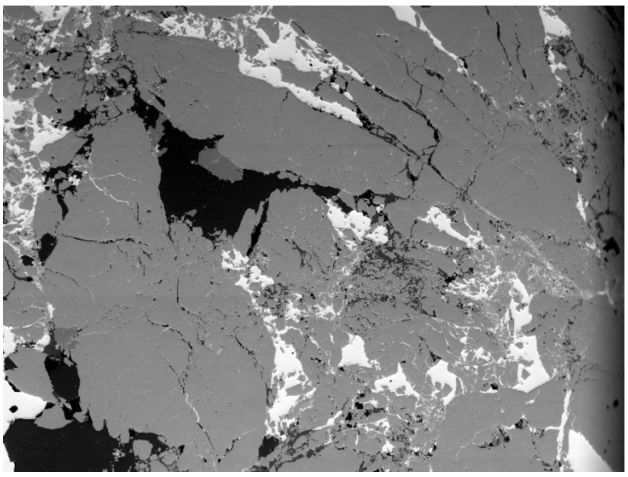

a) BSE image derived from raw EBSD patterns.

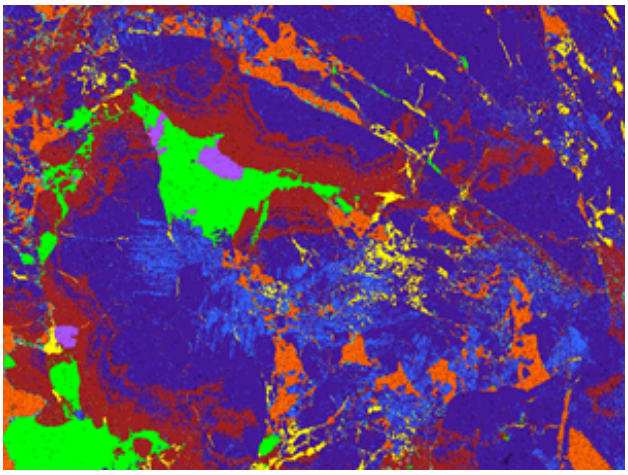

b) Phase distribution map by EBSD + EDS.

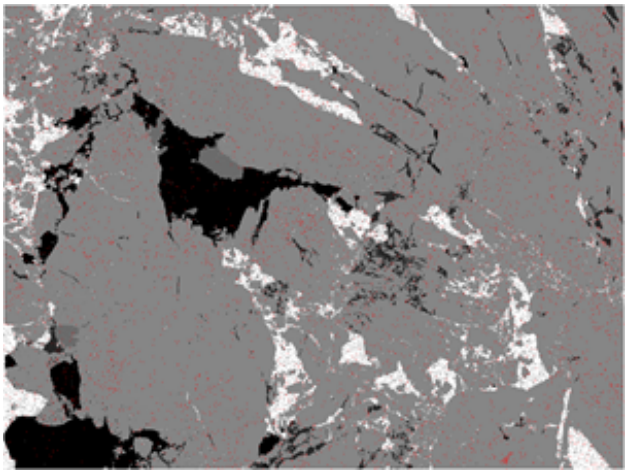

c) Phase distribution map of (b) but using η for gray-scaling.

Figure 4 Microstructure of a rock (mining waste from Saxony/Germany) containing arsenic and bismuth rich minerals. (a) is an image derived from the intensity of the raw EBSD signal. Bright pixels describes positions where patterns with a high background signal have been collected (high $\bar{Z}$) whereas at dark pixels the raw EBSD signal was lower (lower $\bar{Z}$).
The phase distribution map in (b) is colorized as follows: yellow: SiO_2, green: CaF_2, purple: ZnS, brown: $CoAs_2$, violet: $NiAs_2$, blue: $NiAs_2$, cyan:Bi_2S_3, orange: Bi.
In (c) the phase distribution of (b) is gray-scale encoded by the respective η, cf. Tab. 2. The single red dots reflect positions where an indexing by EBSD was impossible.
The mapped area has a dimension of 3.87×2.9mm.

of a mining waste investigated at low magnification. This mineral waste disposal is rich in arsenic and bismuth, and a possible risk caused by weathering needed to be evaluated. The combined EBSD/EDX map has been performed as single scan covering an area of $\approx 4 \times 3$ mm. Each image pixel in Fig. 4 (a) represents the accumulated intensity of the top area exemplarily marked in yellow in Fig. 2 (b). The shading losses at the right edge are, in fact, minor and caused by the last aperture of the SEM. The so derived BSE image reflects three groups of phases. We have strongly backscattering phases (bright, high $\bar{Z}$), phases which are gray (intermediate $\bar{Z}$), and phases which have a lower backscattering power (dark, low $\bar{Z}$). As long as we do not have any information about at least two phases, any absolute correlation between gray-scale and $\bar{Z}$ is impossible.

Firstly, we need to select a set of reasonable phases using EBSD and if necessary EDX. They are listed in Table 2 and marked as well in Fig. 3. It becomes clear that dark areas in Fig. 4 (a) qualitatively correlate with quartz (SiO_2) or fluorite (CaF_2). According to Table 2 sphalerite (ZnS) and all arsenides ($NiAs_2$, $CoAs_2$) have similar η so that they obviously form the gray-colored areas, whereas Bi and Bi_2S_3 are at the upper range of η so that they fit to the white regions in (a).

For a plausibility check of the selected phases we can use the phase distribution map in Fig. 4 (b). It follows from the indexing and phase assignment using the BKD patterns, i.e., the remaining signal after background processing. For this specific material, EDX is only required for a differentiation between the cubic phases fluorite and sphalerite. All other phases can be easily discriminated by their BKD patterns. In order to evaluate the phase recognition, the phase map in (b) can be colored in gray-scale using the phase specific η as scaling factor. This is shown in Fig 4 (c). Only a good correlation between (a) and (c) indicates a correct selection and recognition of phases. If a phase would be incorrect, e.g. because of missing crystal water or OH groups, clearly different contrasts should appear.

The mutual misinterpretation of fluorite and sphalerite patterns nicely demonstrates that an indexing of BKD pat-

Table 2 Backscatter coefficient η as function of the mean atomic number $\bar{Z}$ – equ. (2) – for phases predicted in Fig. 4. The values are used for the gray values in Fig. 4 (c) and marked in Fig. 3.

Phase	Quartz SiO_2 trigonal	Fluorite CaF_2 cubic	Sphalerite ZnS cubic	Clinosafflorite $CoAs_2$ monoclinic	Rammelsbergite $NiAs_2$ orthorhombic	Pararammelsbergite $NiAs_2$ orthorhombic	Bismuthinite Bi_2S_3 orthorhombic	Bismuth Bi trigonal
$\bar{Z}$	10.8	12.7	27.5	31.3	31.6	31.6	70.5.0	83.0
η	0.127	0.172	0.275	0.319	0.321	0.321	0.469	0.496

terns with a high confidence does not automatically indicate a correct phase assignment, indexing and orientation determination. Since EDX spectra have been acquired simultaneously, both phases can be differentiated by the characteristic X-rays emitted. However, the different η would also enable a phase discrimination without any EDX information. Moreover, a dwell time of e.g. 30ms or less does not enable a detection of all element-specific radiation components with a comparable statistical significance, and some light elements are not even detectable by EDX. Here the BSE signal can be a sufficient and perhaps also more reliable alternative.

Please note that the *absolute* number of η is not necessarily requested for a discovery of wrong candidates in a phase list. Often it is sufficient to separate phases only by their gray-scale difference.

It is worth to remember that the BSE signal is also available for amorphous or nano-crystalline phases which do not form any or only an occasionally detectable BKD signal.

3.3.2 High spatial resolution As long as the grain size is clearly larger than the resolution of EDX, the EDX signal is sufficient for the short dwell times typically used during EBSD mapping, and the phase-specific radiation components are clearly separated, EDX can be applied as phase discriminator. However, already if microstructure features become smaller than the information volume of EDX, the chemical signal is blurred and becomes unsuitable for a pixel-precise phase differentiation.

A typical example is given by the γ/γ' microstructure in Ni-base superalloys which consist of a face-centered cubic (fcc) γ matrix with a high volume fraction of γ' precipitates (ordered $L1_2$ structure). The different ordering comes along with a minor change of the lattice parameter only. However, many properties of this material are related to the very specific precipitation hardening. Therefore, a correct knowledge about the phase fraction is essential.

Transmission electron microscopy easily resolves the microstructure and differentiates between both phases but the covered area is of low statistical significance.

Evaluation of the microstructure in the SEM works after phase-selective etching but the imperfect selectivity as well as imaging artifacts call the reliability of an exact determination of the volume fraction into question. Moreover, both techniques require a destruction of the material. Investigations with EDX in the SEM are possible but the small size of the precipitates allows a rough phase recognition only. Therefore, an imaging of sharp phase boundaries by EDX at for EBSD typical acceleration voltages is practically impossible.

EBSD possesses the requested spatial resolution but the BKD patterns of both phases look practically identical. Also, a qualitative consideration of the higher dislocation density in γ compared to γ' and its impact on the pattern quality is not sufficient for an unequivocal phase discrimination. Because of the coherent interface between γ and γ' also no clear phase boundaries appear in the pattern quality map. However, if one uses the raw BSE signal the differences in chemical composition are sufficient to deliver significant contrast from high-resolving EBSD maps, cf. Fig. 5. The reason for this surprisingly strong contrast becomes evident if one compares the nominal composition with the composition of γ and γ' after standard heat treatment, cf. Table 3. During precipitation an inverse segregation of some heavy (Re and Ta) and light elements (Al) happens which generates this clearly different BSE signal. η for γ and γ' are also displayed in the diagram in Fig. 3.

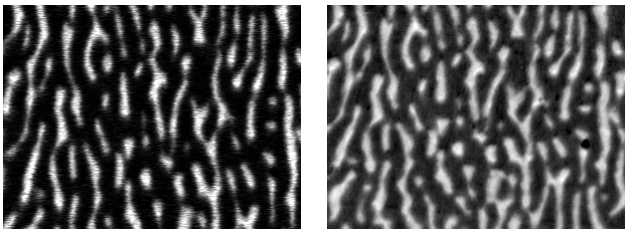

a) hardware BSE image b) from raw EBSD signal

Figure 5 Discrimination of γ (fcc, bright) and γ' ($L1_2$, dark) in CMSX-10 by a hardware BSE detector (a) or the upper part of the raw EBSD signal (b). A phase assignment during EBSD mapping by (a) is impossible because of the image drift visible in (b). (map size: 300×225 pixels (12.6×9.45µm), step with: 42nm)

A more serious problem during orientation mapping is image drift preferably visible at high magnification. Even if the backscattered signal from a BSE hardware detector is sufficiently different for both phases, the captured image before or after the mapping does not necessarily match the final EBSD scan, cf. Fig. 5 (a) and (b).

3.3.3 Small differences in $\bar{Z}$ In Fig. 4 chemically extremely diverse phases were the reason for a strong spread of η. Therefore, several phases with small $\Delta\eta$ are displayed by a similar gray level. However, this does not

Table 3 Nominal composition of the nickel-base superalloy CMSX-10 and composition of γ and γ' after standard heat treatment in mass fraction and concentration [32].

		Cr	Co	Mo	Al	Ta	W	Re	Ni	$\bar{Z}$
nominal	wt%	2	3	0.4	5.7	8	5	6	69.9	
	at%	2.4	3.2	0.3	13.2	2.8	1.7	2.0	74.5	35.8
γ	wt%	5.8	7.6	0.7	1.0	1.0	6.5	22	55.4	
	at%	8.0	9.3	0.5	2.7	0.4	2.5	8.5	68.0	41.4
γ'	wt%	1.1	2.0	0.3	6.5	11.1	4.8	1.6	72.6	
	at%	1.3	2.1	0.2	14.8	3.8	1.6	0.5	75.8	35.0

mean that their separation is in general impossible. Often already a definition of a smaller η range proves that such phases can be distinguished. A reliable differentiation between $NiAs_2$ and $CoAs_2$ by η is admittedly an illusion since their calculated η values are practically identical, cf. Table 2. However, ZnS can be discriminated, cf. Fig. 4, and also quartz and fluorite show after re-scaling clearly different gray values. Having the decreasing sensitivity with increasing Z in mind (Fig. 3), as rule of thumb, the gray values between two phases can be distinguished and used as discriminator if

$$\Delta\bar{Z} > 1.$$

Essential is of course the signal-to-noise ratio, i.e., mainly the dwell time used.

In general, a phase discrimination by the BSE signal becomes challenging if surface topography and/or the degree of channeling cause an intensity variation which is comparable to $\Delta\bar{Z}$ of the contributing phases. Especially surface topography is crucial since during preparation of a multiple-phase material it practically cannot be prevented. A small topography will be even amplified by the tilt-specific image correction $\propto 1/\cos\chi$ ($\chi \ldots$ tilt angle). Therefore, the top priority during sample preparation is a smallest possible implementation of preparation artifacts combined with a minimum of surface topography.

The simultaneous acquisition of EBSD and EDX still forces the user to increase the dwell time in order to collect enough counts for a spectral evaluation of the EDX signal. This has positive side effects on the BSE intensity variation since it simultaneously increases the signal-to-noise ratio. But already a comparison of the dwell time used for a common imaging with the dwell time applied during EBSD-pattern acquisition explains the clear noise difference.

However, if within a grain the noise of the BSE intensity is smaller than the channeling signal above the background level, different crystal orientations appear. This is visible in BSE images of a single-phase material where $\eta = \text{const}$. It means that if the intensity change caused by channeling is larger than $\Delta\eta$ of two phases, a phase discrimination is limited. Nevertheless, under specific circumstances even a small $\Delta\eta$ enables a phase discrimination, e.g. for Fe oxides.

Wuestite – Magnetite transformation During transformation from wuestite (FeO) to magnetite (Fe_3O_4) the describing translation lattice remarkably changes ($a_W = 4.341$Å, $a_M = 8.393$Å) but the basis-vector directions stay unaffected. The structural similarities (a very little changed Fe distribution in a practically invariant closed-packed framework of O atoms) are the reason that a high number of Kikuchi bands does neither change intensity nor width[2]. Only some less intense and narrow bands, resulting from the approximately doubled unit cell dimension of magnetite, make a phase assignment possible. The improvement of the BKD quality by frame averaging during acquisition reduces the amount of phase misinterpretation but it cannot prevent it entirely. A simultaneously collected EDX signal as used for the upper examples does not help since the marginally different chemical compositions are insufficient for a phase discrimination. However, the same chemical compositions are suitable enough to deliver a sufficient gray-value difference of the BSE signal, see Fig. 6 and Table 4.

Table 4 Mean atomic number $\bar{Z}$ and backscatter coefficient η for some corrosion products of iron.

phase	$\bar{Z}$	η
FeO	22.0	0.245
Fe_3O_4	21.0	0.236
Fe_2O_3	20.6	0.232
FeOOH	19.2	0.220

The surface topography in Fig. 6 (a) does not remarkably affect the application of a simple thresholding (b) which makes a successful assignment of wuestite (white pixels) and magnetite (black pixels) possible.

However, Fig. 6 displays a single-crystalline region. If more grains are mapped, the orientation specific channeling signal can become bigger than the gray-value difference caused by $\Delta\bar{Z}$ of FeO and Fe_3O_4. In this case a grain-specific thresholding helps since for each grain $\Delta\bar{Z}$ is clearly detectable. Thus, in a first step the grains need to be determined using their orientation. To this end, the microstructure will be indexed by only one phase, e.g. by wuestite. In a second run, within each grain the BSE

[2] This is also the case during transformation from magnetite to hematite (Fe_2O_3) [33].

a) BSE image derived from the raw EBSD signal

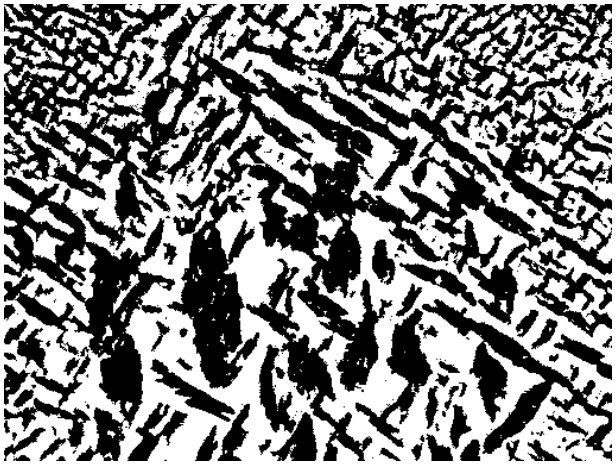

b) after thresholding of (a)

Figure 6 Discrimination of wuestite (FeO, bright, $\bar{Z} \approx 22$) and magnetite (Fe_3O4_4, dark, $\bar{Z} \approx 21$) using the upper part of the raw EBSD signal collected during combined EBSD and EDX mapping. Caused by their crystallographic relationship the BKD patterns can be indexed by only one phase since the phase assignment is controlled by the raw intensity only.
(map size: 77×58µm)

thresholding can be applied to assign all dark pixels to magnetite.

In Table 4 also further corrosion products of Fe are listed. $\Delta\bar{Z}$ between magnetite and hematite are only 0.4 so that a reliable discrimination of these two phases by η is unlikely, especially when surface topography exists. Fortunately, the pattern correlation is not that strong as for magnetite and wuestite so that a separation by EBSD only is not problematic [33]. Also FeOOH – goethite (α), akaganeite (β), lepdocrocite (γ) – shows a clear difference in $\bar{Z}$ so that BSE in combination with EDX can be used for an identification of FeOOH if no or only locally BKD patterns are available.

3.3.4 Signal correlation Assuming a sufficient stability of the SEM, BSE images derived from raw EBSD patterns are in general of higher quality than images captured with a real BSE detector. The primary reasons have been already mentioned: the longer dwell time per pixel, the bigger solid angle, and the passive energy filtering caused by the aluminum coated phosphor. The time spent for a subsequent re-processing is worth the effort.

Analytically of higher interest is the direct correlation of the Kikuchi diffraction (KD) and the background (BG) signal derived from the same pattern. The first tells us something about the crystallography of the phase and the second something about the chemical composition of the phase. There is neither a systematic shift at higher magnification as known for EDX (different information volume and tilt), nor a non-predictable drift as common for subsequently acquired measurements and mainly caused by local charging.

3.4 Orientation contrast imaging It has been argued that the forescatter diodes (FSD) mounted *below* the EBSD screen collect a signal which is dominated by the crystal orientation [7], which can provide important qualitative orientation information.

For imaging, a various number of FSDs can be used. The signal of a single FSD can be converted into a gray-scale image as shown in Fig. 7 (a). DAY & QUESTED [11], proposed a signal mix of three separate detectors in order to improve the orientation sensitivity by false-color images, cf. Fig. 7 (b).

The pixel color depends in a non-trivial way on phase parameters like composition, crystal structure and crystal orientation, cf. Fig. 7 and 8. Also the specifically chosen imaging conditions like the relative alignment of detector and sample (including sample and detector tilt, detector-sample as well as working distance), the acceleration voltage, the magnification, and the surface topography have an essential impact on the signal mix and therefore on the resulting color. In effect, a small change of any parameter can cause tremendous color variation. Therefore, observable color variations only indicate a local change of the BSE signal but there is no meaningful quantification regarding the crystal orientation or with respect to the inherent misorientation. An abrupt color change can indicate small-angle boundaries in the scale of tenths of a degrees just as well as it can express high-angle boundaries. Especially during pre-assessment of a microstructure by a hardware detector like ARGUS™ colored images are more suitable than gray-scaled images, cf. Fig. 8.

3.4.1 BKD imaging Using the saved raw EBSD pattern, we have access to the background as well as to the separated BKD signal by image processing [34]. This allows further imaging modalities. In Fig. 9 the results of a simple image processing at the example of a quartz pattern are compared. In (a) the raw signal is displayed. Applying a FFT low-pass filter on (a) the diffraction signal practically disappears and we get in (b) the non-modulated part

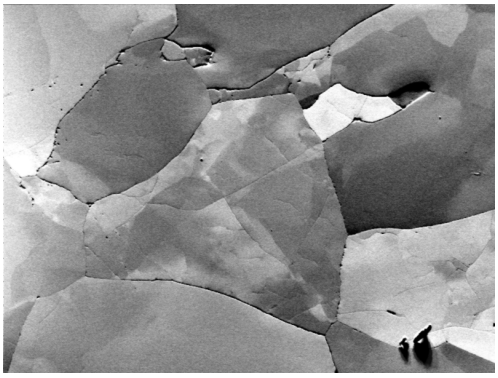

a) single FSD

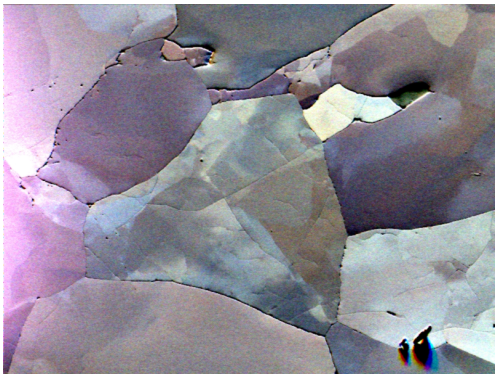

b) triple FSD (ARGUS, Bruker)

Figure 7 Microstructure of a quartzite. (a) shows a typical gray-scale image collected by a single-diode FSD. If three detectors as in Fig. 2 are combined false-color images can be created (b). (map size: 797×598µm).

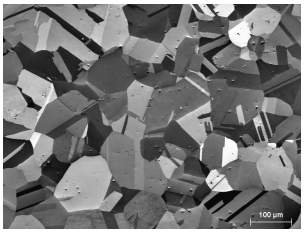

a) single FSD

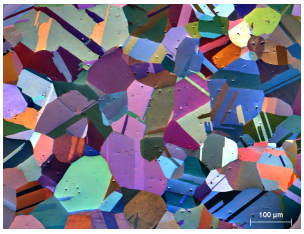

b) triple FSD (ARGUS™)

Figure 8 Polycrystalline nickel captured by a single element detector (a) and a triple detector (b) generating false-color images. The more pronounced the channeling-in signal the more brilliant the color variations. (image size: 720×540µm)

of (a). Dividing or subtracting (a) by/from (b) the modulated signal (c) results. Here, it becomes clear how small the modulated signal on the background really is since the same intensity scaling as for (a) and (b) is used. A re-scaling delivers the BKD pattern (d) which is commonly displayed in the acquisition software and applied during

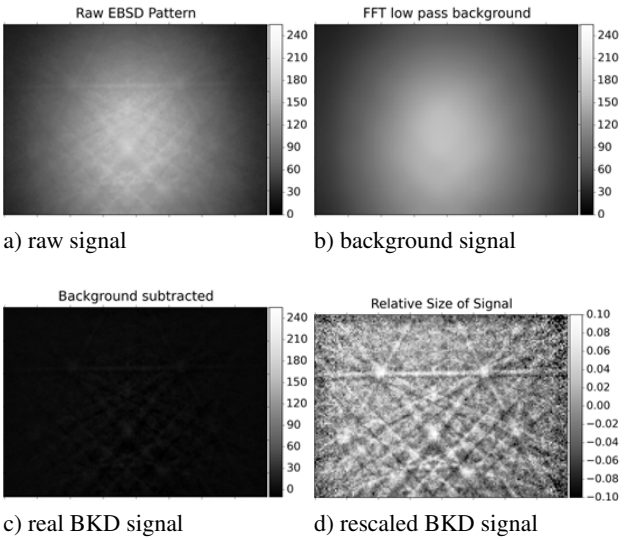

a) raw signal b) background signal

c) real BKD signal d) rescaled BKD signal

Figure 9 Processing of a raw EBSD signal (160×155 pixels) collected at quartz 16 ms (20 kV, 7 nA, cf. Table 1).

Hough transformation, band indexing and orientation determination. The legend in (d) represents the signal fraction and runs from $-0.1 \ldots +0.1$. Effectively, it shows that the BKD signal of quartz is not higher than $\pm 5\%$ compared to the raw BSE signal, and that the noise amplitude is larger than the dynamic of the BKD signal itself (the size of the BKD contribution can be higher for other materials, reaching values near 20% in favorable cases). A further averaging of patterns would only reduce the noise amplitude but not the amplitude of the BKD signal above the background.

In order to emulate a triple FSD as proposed in [11], areas similar to the red, green and blue colored regions in Fig. 2 (b) have to be selected. Equivalent to the $\bar{Z}$-contrast images generated above, now three images have to be derived, re-scaled and mixed to a color image. For the central quartz grain in Fig. 7 this has been done and is shown in Fig. 10. In (a) and (b) the raw EBSD patterns have been used, in (c) and (d) exclusively the BKD signal is considered, i.e., the background signal has been removed from the raw BSE signal. The images in (e) and (f) are generated by the previously removed background signal only.

At first glance there seems to be no big differences. All images look colorful. In accordance to [16, 14] the images in (a) and (b) only confirm that by using the raw EBSD patterns FSD-like images can be generated.

More important and of huge consequences are the images (c) and (d) in Fig. 10. Although the BKD or channeling-out signal delivers a similar image, the higher noise level, nicely visible in (d), indicates that the intensity of the BKD pattern is of comparable magnitude only. This cannot explain the very sensitive and noise-poor FSD images. If BKD would be the dominating effect, the image quality in (c) and (d) should be at least that good as shown in (a) and (b).

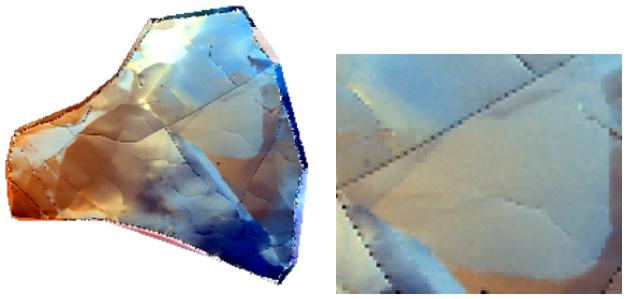

a) raw signal (Fig. 9 (a)) b) detail of (a)

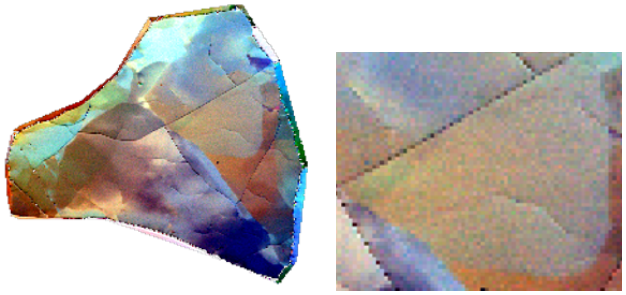

c) background-processed BKD signal (Fig. 9 (d)) d) detail of (c)

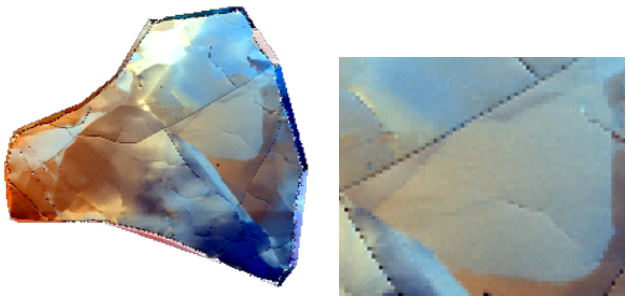

e) background signal (Fig. 9 (b)) f) detail of (e)

Figure 10 Impact of the raw EBSD (a+b), the modulated BKD (c+d), and the non-modulated background signal (e+f) on derived false-color images. Raw and background signal deliver practically the same image. The image of the diffraction signal, however, only looks similar. The noise indicates that the visible image is the remaining part of the imperfect background reduction.

Quite surprising are, however, the images derived from the background signal and displayed in Fig.10 (e) and (f). The direct comparison with (a) and (b) indicates that there are practically no differences. From this follows that the background signal must be the major component for the orientation contrast visible in FSD images. Thus, the FSD signal is mainly formed by channeling-in and not by channeling-out. The still visible signal in Fig.10 (c) and (d) is very likely a residual part from the background processing using FFT filtering. This also fits to the raw-signal partitioning in Fig. 9 (b+d) and to the previous discussion about the contribution of KD and BG to the EBSD pattern.

Overall, these results indicate the impact of incident beam diffraction effects, which also explain the extremely angular sensitivity of FSD images. The same channeling-in effects are also responsible for the recent renaissance of electron channeling contrast imaging (ECCI) [35–37].

3.5 Higher order image properties: Center of intensity Incident beam diffraction [38] as well as the surface topography [39] change the directional distribution of the backscattered electron signal. This variation is very small but can be imaged for example by the calculation of the center of intensity (COI) of the measured images. We define the center of intensity as the intensity-weighted mean of pixel positions. For a demonstration of COI imaging, the dataset of the quartz grain is used again and the result is shown in Fig. 11 (a). The applied color scheme

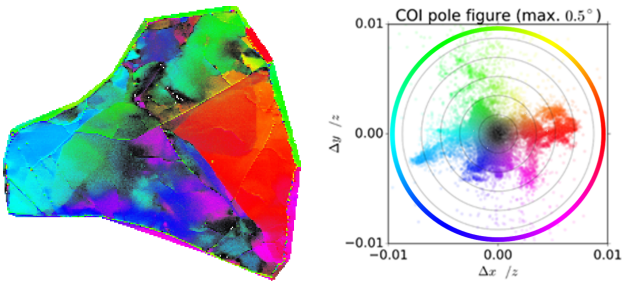

a) COI map b) COI pole figure

Figure 11 Center of Intensity (COI) applied on the quartz grain shown in Fig. 10. The colors describe a change of the mean intensity direction (b) which is due to channeling-in and topography effects. The color distribution runs from black (no deviation to the center) to a direction-dependent color, cf. the color circle.

in (a) describes the azimuthal deviation (rainbow colors) whereas the polar deviation to the mean value is encoded by the brightness (b). The derived microstructure features in Fig. 10 and 11 look very similar. However, whereas in Fig. 10 the visible color variation does not reflect any quantitative information the variation of COI displays a misorientation description in a very high precision ($-0.01 \leq \Delta x/z, \Delta y/z \leq 0.01$)[3]. Compared to the pattern resolution of 160×120 pixels the shown $\Delta x/z = 0.01$ approximately represents a single pixel. The precision is in first approximation about a tenths of a pixel.

From the COI pole figure in Fig. 11 (b) the misorientation axis as well as the misorientation angle can be derived. The COI pole figure in (b) only displays the deviation from a still unknown orientation, but assuming an orientation determination by EBSD the angular deviation can be used to characterize the visible subgrain boundaries in an at least semi-quantitative way. For single-grain materials this opportunity can be very powerful. For a general application on polycrystalline materials it still needs further evaluation.

[3] Δx and Δy describe the deviation of COI on the screen whereas z defines the screen-sample distance

In conclusion, FSD images as well as COI maps are useful tools for a visualization of misorientations with remarkable sensitivity. However, since these maps are mainly determined by the background signal, any kind of quantification is not straightforward and requires the diffraction signal for a most accurate orientation description. Therefore, we have investigated advanced approaches to obtain the crystal orientation from the BKD patterns with a higher accuracy and precision as well.

4 Quantitative post-processing of BKD patterns

The orientation precision of conventional EBSD is typically estimated to be in the scale of $0.5\ldots1°$. For an orientation characterization this precision is more than sufficient [40]. However, for the determination of small misorientations optimized or totally new approaches are required. The use of higher resolved BKD patterns seems to be a straightforward option to improve accuracy and precision of band positions and widths, however, it is not clear, how exactly the applied software packages internally process high-resolution patterns. Typical questions are related to thresholding, software-internal binning of patterns, adaptation of size and shape of the butterfly filter etc. In any case, the disadvantage is at least a clearly longer acquisition time which means unusual stress on sample and equipment. Therefore, the question arises whether there are alternative ways increasing the orientation precision using BKD patterns with standard resolution (i.e. 160×115 pixels in our case)?

4.1 Orientation refinement by pattern matching

The pattern matching approach we use is based on the cross-correlation coefficient between two images, the experimental and a simulated pattern, with a starting solution given by the standard Hough-base indexing result. The work flow is sketched in Fig. 12. For each experimental BKD pattern, the orientation and possibly the detector parameters are optimized using a downhill simplex approach searching for the largest cross-correlation coefficient.

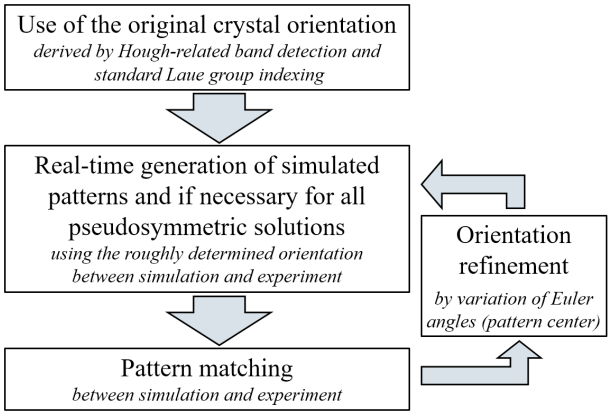

Figure 12 Workflow principle of the pattern-matching procedure.

The difference of our approach to dictionary-based techniques used for indexing of selected area electron diffraction (SAED) pattern in TEM [41], or of BKD patterns in SEM [42–44] is the individual re-projection of the master data for arbitrary parameters in each optimization step, without a fixed set of dictionary parameters. This approach is possibly slower than the dictionary-based techniques, but it is not limited by the resolution of the pattern dictionary.

Besides the improvement of the orientation precision pattern matching enables a wide range of not immediately evident applications like the solution of pseudosymmetry problems, the correct indexing of non-centrosymmetric phases, and an improved phase discrimination.

4.2 Increase of orientation precision

A high orientation precision is important for many kinds of misorientation and strain analyses using EBSD [45–51].

In Fig. 13 three different misorientation tools are used to compare the precision of the original orientation data with the precision of the refined orientation descriptions. For this example, we analyze the same quartz measurement as above.

In (a) and (b) the local misorientation angle to the mean orientation of the grain (GAM... grain average misorientation) is given. Within this grain maximum misorientation angles of $\approx2°$ occur. Both, the original as well as the refined data show qualitatively similar maps. A closer look, however, indicates that in (b) more subgrains appear more clearly. This is caused by the lower noise in (b) so that systematic misorientations smaller than the orientation noise can be discovered. This is similar for the *kernel average misorientation* (KAM) maps in (c) and (d). The KAM visualizes the local orientation gradient. For each pixel of a grain it reflects the mean misorientation within the surrounded kernel. The KAM maps in (c) and (d) look qualitatively and quantitatively different. Firstly, parts of the subgrain boundaries are not always discovered before refinement, and secondly, the KAM map of the original orientation data suggest subgrains which are characterized by higher local misorientations than other subgrains. However, as (d) shows, all subgrains are characterized by a comparable KAM of $0\ldots0.2°$, and the misorientation between the subgrains are in the range of $0.4\ldots0.5°$ only. With respect to the precision of the misorientation angle, the refined orientation data shows a maximum at $0.2°$ whereas for the original orientation description a misorientation-angle distribution delivers a maximum at $\approx0.6°$, i.e., a reanalysis of the same patterns improves this value by a factor of three.

The maps in Fig. 13 (e) and (f) show the misorientation angle and direction by coloring a selected reference direction in terms of the inverse pole figure (IPF). However, since the IPF color key would be too insensitive to reflect these small misorientations, an adapted IPF key is used. It colorizes the mean vector $[u\,v\,w]$ in white, and any deviation uses an MTEX-specific color distribution as given

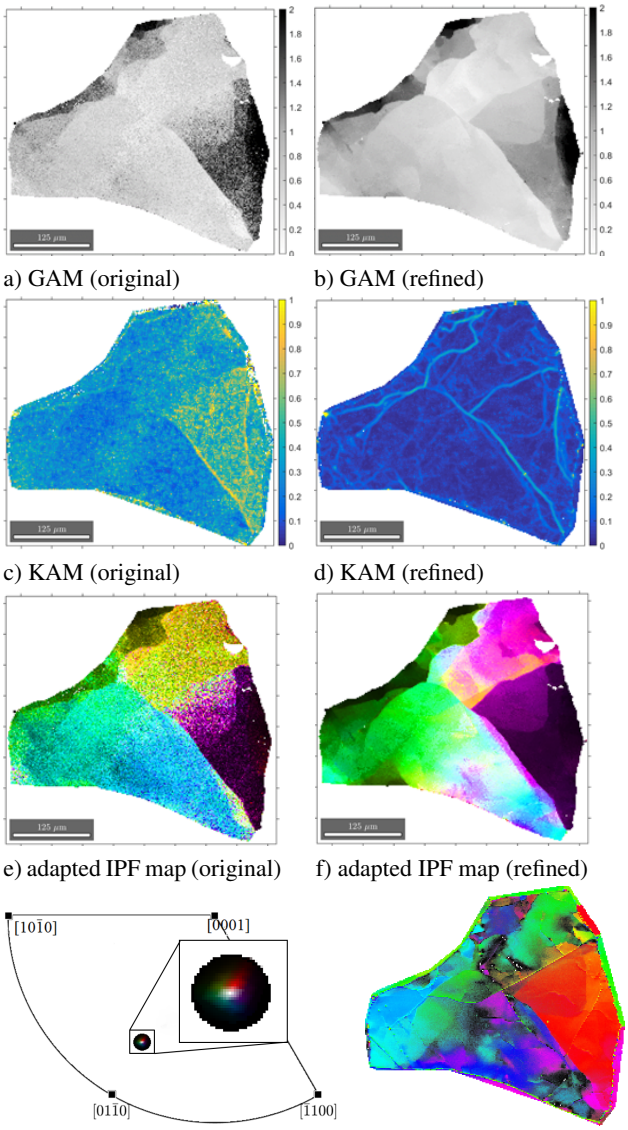

a) GAM (original) b) GAM (refined)

c) KAM (original) d) KAM (refined)

e) adapted IPF map (original) f) adapted IPF map (refined)

g) adapted color key for (e) and (f) h) COI (Fig. 11).

Figure 13 Impact of pattern matching on the orientation precision. The misorientation to the average orientation of the grain (GAM) as well as the kernel average misorientation (KAM) show a distinctively lower misorientation noise for the refined orientations. For the IPF coloring in (e-g) an adapted color key of MTEX has been used, cf. (g). There the mean of the reference direction X=[1,0,0] is drawn in white. Azimuthal deviations (0...360°) are encoded in rainbow colors whereas polar distances (0...2°) running from white to black. For comparison in (h) the semi-quantitative COI map is shown.

in (g). It is obvious that (e) and (f) reflect a considerable difference in precision between original and refined orientation data as well. Also of interest is the comparison of the quantitative misorientation presentation with the semi-quantitative COI map of Fig. 11. Despite the different color

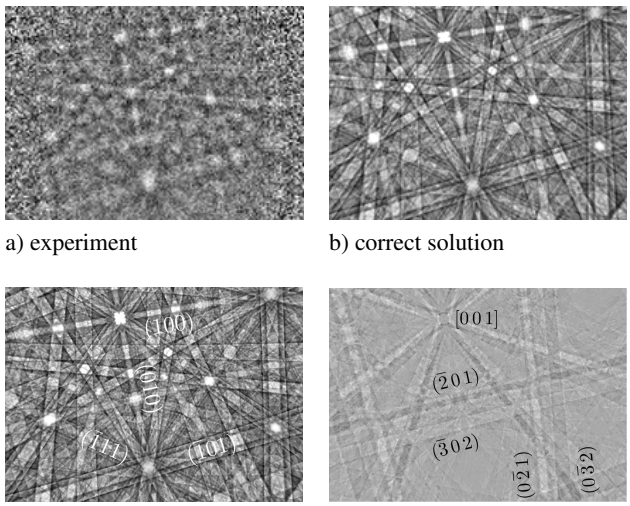

a) experiment b) correct solution

c) wrong solution d) difference signal (b-c)

Figure 14 Comparison of experimental and two pseudo-symmetric simulated patterns of pyrite. The intensity difference between both solutions are shown in (d) using the same scaling as for (b) and (c). For guidance, in (c) and (d) a few lattice directions and planes are given.

key used a qualitative match between both images is visible.

Summarizing, post-processing of high-binned EBSD patterns significantly increases the orientation precision of orientation measurements and improves the reliability of misorientation-related investigations like the estimation of the amount of geometrically necessary dislocations (GND).

4.3 Pseudosymmetry

4.3.1 Centrosymmetric phases Since there are 11 Laue groups but 6 translation lattices only, some Laue groups need to share the translation lattice. Because the symmetry of the crystal lattices coincide with the higher symmetric Laue groups, for the low-symmetric Laue groups $m\bar{3}$, $6/m$, $\bar{3}$ and $4/m$ the higher symmetry of the respective crystal lattice is suggested. A typical example is given by Pyrite (FeS_2) [52].

Example: Low-symmetric Laue group Pyrite is a cubic phase. The crystal lattice suggests a four-fold rotation symmetry along $\langle 0\,0\,1\rangle$. However, the crystal structure of pyrite matches to space-group type $P\,2_1/a\bar{3}$ which does not contain any four-fold rotation or screw axis but only a two-fold rotation $\|\langle 0\,0\,1\rangle$. Practically it means that e.g. the lattice planes $(1\,2\,0)$ and $(\bar{1}\,2\,0)$ are not symmetry-equivalent although their interplanar distances are identical. The missing four-fold rotation symmetry can by only expressed by the intensities of the respective bands as result of the crystal structure, i.e., the phase-specific configuration of atoms. The impact of the structure on the intensity distribution is demonstrated in Fig. 14.

A typical experimental BDK pattern (a) is compared to two pseudosymmetric solutions, (b) and (c). In order to recognize the differences between both simulations, the intensity difference is shown in (d). The intensity scale for (b)-(d) is identical which shows in (d) that the difference between both solutions is firstly small, and secondly limited on a few bands only. The visible intensity differences are caused by $\{2\,1\,0\}$ (narrower bands) and $\{2\,3\,0\}$ (broader bands) since interferences of $\{1\,2\,0\}$ and $\{3\,2\,0\}$ are absent in this space-group type. The intense bands of $\{1\,0\,0\}$, $\{1\,1\,0\}$ and $\{1\,1\,1\}$ are totally symmetric. They de facto display the non-existing four-fold pseudosymmetry of the lattice, and consistently disappear in (d). Since the intensities of $\{2\,1\,0\}$ and $\{2\,3\,0\}$ are small, a systematic misindexing occurs for pyrite, especially when the BKD signal is noisy and $\{2\,1\,0\}$ and/or $\{2\,3\,0\}$ are hard to detect.

For a demonstration framboidal pyrite has been investigated [52]. The IPF map in Fig. 15 (a) reflects numerous pyrite grains smaller than 1µm. Many of them are not uniformly colored which indicates a systematic misindexing. An IPF coloring of more than a single reference direction would show that practically all grains are described by two non-equivalent orientation solutions. The standard indexing obviously generates random but also systematic misinterpretations which depend on the crystal orientation. There is no other way to explain the totally or nearly completely misindexed grains which are marked by black circles. White pixels are positions where the BKD pattern could not be indexed (pixel size: 60nm, cf. Table 1), or the match results in a cross-correlation factor $r < 0.3$.

The challenge is now to decide which of the two pseudosymmetric solutions within a grain is correct? This is achievable by pattern matching if the experimental pattern will be compared with the simulated patterns of both pseudosymmetric orientation solutions. This solution with the better cross-correlation coefficient r ($0 \leq r \leq 1$) is selected as most probable. In order to get the best correlation between experimental and simulated pattern the orientation will be refined first, and in a second step the pseudosymmetry test will be carried out. The re-processing results

An alternative way to the previously described would be the indexing of all patterns by a phase which represents the higher-symmetric Laue group, e.g. $\gamma-$Fe. The resulting grain orientations are then either correct or wrong but the speckled grains as shown in Fig. 15 (a) will disappear. The subsequent pattern matching will then change the orientation of entire pyrite grains if necessary, cf. the map in Fig. 15 (b). This is probably the even better and faster way since the grains are identified already during the first run. The simultaneous increase of the indexing rate in (b) compared to (a) only indicates that the standard indexing algorithm for pyrite is improvable since for $\gamma-$Fe the hit rate is remarkably better.

Please note that the applied IPF coloring is based on the in Fig. 15 (c) shown asymmetric sector of the enantiomorphic symmetry group 23, and not on point or Laue group $m\bar{3}$. A coloring by the respective enantiomorphic point group is highly recommended since the application of the commonly used Laue group encodes mirror-symmetric orientations by the same color so that differently oriented grains cannot be visually distinguished [53].

a) Hough-related "standard" indexing (scale bar: 2µm)

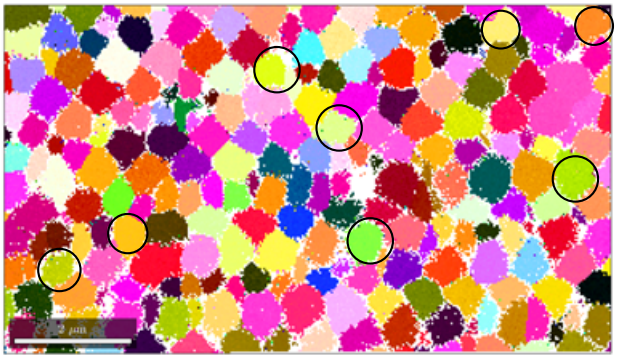

b) wrong solutions removed by pattern matching

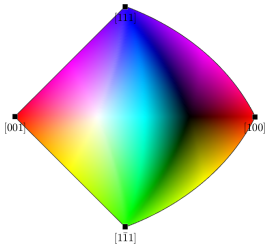

c) IPF color key for 23 [53]

Figure 15 IPF maps of framboidal pyrite [52]. Comparison of the map using standard indexing (a) with the indexing by pattern matching (b). The applied IPF color key (c) assigns red to the symmetry-equivalent $[0\,0\,1]$ and $[1\,0\,0]$ but distinguishes correctly between $[1\,\bar{1}\,1]$ (green) and $[1\,1\,1]$ (blue).

4.3.2 Non-centrosymmetric phases In some applications non-centrosymmetric materials are relevant, e.g. where crystal properties like piezoelectricity or pyroelectricity are beneficial. Sometimes only non-equivalent orientations need to be discriminated in order to characterize microstructure defects. Unfortunately, present EBSD systems are not able to index BKD patterns with respect to their point-group symmetry, althogh already in 1989 BABA-KISHI and DINGLEY showed that Friedel's rule is not valid for EBSD [54].

Example: Zincblende-type structures Cubic semiconductor compounds of type $A^{III}B^{V}$ like GaAs, GaP, InP etc. crystallize in the non-centrosymmetric structure type of sphalerite (ZnS, space-group type $F\bar{4}3m$, IT-No: 216). One peculiarity of non-centrosymmetric structures is that lattice planes exist which are polar, i.e., upper and lower side have different properties,cf. Fig. 16 (a).

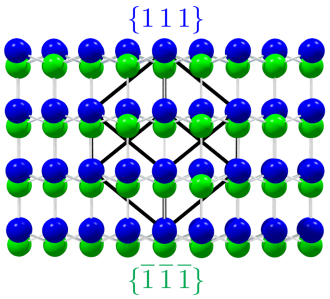

a) Different stacking of atomic layers along opposite directions $\langle 1\,1\,1\rangle$ and $\langle \bar{1}\,\bar{1}\,\bar{1}\rangle$ displays the diverse polarity of $\{1\,1\,1\}$ and $\{\bar{1}\,\bar{1}\,\bar{1}\}$.

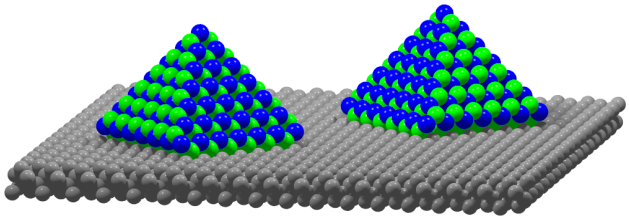

b) Two around 90° rotated nucleus with $\{1\,1\,1\}$ (mainly blue) and $\{\bar{1}\,\bar{1}\,\bar{1}\}$ (mainly green) habit planes on a $(0\,0\,1)$-oriented centrosymmetric substrate, e.g. Si.

Figure 16 Polarity character of planes in non-centrosymmetric zincblende-type structures (a). The heteroepitaxial growth on a centrosymmetric substrate ends in two pseudosymmetric orientations which cause the formation of antiphase domains.

Since polar lattice planes generate asymmetric intensity profiles across the formed band, this asymmetry can be used to differentiate between A and B-side, i.e., for example between $\{1\,1\,1\}$ and $\{\bar{1}\,\bar{1}\,\bar{1}\}$.

The resulting pseudosymmetry has practical consequences for specific applications like epitaxial growth. For example, with respect to a centrosymmetric substrate like Si, a nucleation of two non-equivalent but pseudosymmetric orientations is possible, cf. Fig. 16 (b). An unconstrained growth will mandatorily cause the formation of undesired antiphase boundaries.

Therefore, a correct polarity assignment is of great advantage and needs a calibrated and validated intensity-profile simulation, cf. [55,56]. However, it has to be taken into account that the polarity character of a general lattice plane $(h\,k\,l)$ depends on the definition of the crystal structure and the selected indices h, k, l. If $(1\,1\,1)$ in zincblende is defined as A-polar, then $(1\,3\,3)$ or $(1\,1\,5)$ are A-polar as well whereas $(1\,1\,3)$ and (135) are B-polar [57].

WINKELMANN et al. introduced a full-automated analysis of BKD patterns so that complete orientation maps can be re-processed [55]. This can be even done with BKD patterns binned down to a size of 160×115 pixels, i.e., there are no high-resolution patterns required as used for demonstrations in [54]. For initial attempts in [55] polycrystalline GaP has been selected in order to refute any orientation dependence of the applied polarity discrimination.

4.3.3 Lower crystal symmetries Because of the high crystal symmetry of cubic phases the asymmetric sector of the BKD signal is so small that several of them appear in an experimental BKD pattern. Thus, commonly more than one of those asymmetric bands become visible and enhance the polarity discrimination. However, for all non-cubic phases this is not the case since with 90° for at least one side of the asymmetric sector the angular dimension exceeds the intensity-rich central part of the EBSD screen (typically $\leq$70°).

Controlled by the crystal structure, polar features in BKD patterns of lower-symmetric phases can be inhomogeneously distributed. Therefore, it is interesting to verify whether the algorithm applied on cubic GaP also works for phases of lower symmetry.

Example: Wurtzite-type structures Besides the cubic sphalerite another crystallographic modification of ZnS exists which is called wurtzite. Like sphalerite it is also non-centrosymmetric, but caused by a different stacking sequence of practically the same atomic layers the resulting space-group symmetry is $P\,6_3mc$ (IT-No: 186). Some technically used semiconductor compounds crystallize in zincblende as well as wurtzite structure, e.g. GaN.

GaN is used for power devices and LEDs. As substrate material $(0\,0\,0\,1)$ sapphire (Al_2O_3, $R\bar{3}c$, IT-No: 167) is preferred, i.e., again a centrosymmetric phase. By changing the deposition conditions a polarity inversion of GaN can be achieved, cf. [58]. For demonstration a lateral polarity heterostructure has been mapped, analyzed by standard processing and afterwards reanalyzed by pattern matching. Some derived IPF maps are displayed in Fig. 17.

In (a) the pattern quality (PQ) is shown overlaid by the inverse pole figure (IPF) coloring of the growing direction. PQ indicates a different surface topography. Stripes of smooth surface are interrupted by stripes with a rough surface. Both are assumed to be of different polarity. However, the applied standard IPF-color key for the Laue group $6/m\,mm$ (right, top) only describes $(0\,0\,0\,1)$-oriented hexagonal GaN (red). Unexpected cubic GaN grains of zincblende structure are identified as well, and according to the color key of $m\bar{3}m$ (right, bottom) all grains are colored blue. This confirms the assumed orientation relationship: $(0\,0\,0\,1)_{\mathrm{hex}} \parallel (1\,1\,1)_{\mathrm{cub}}$. All in all, the application of the standard Laue-group coloring is unable to visualize the polarity.

The IPF map in (b) displays the same orientation data of hexagonal GaN but colorized with respect to the point-group symmetry $6mm$. Now the alternating stripes of N-

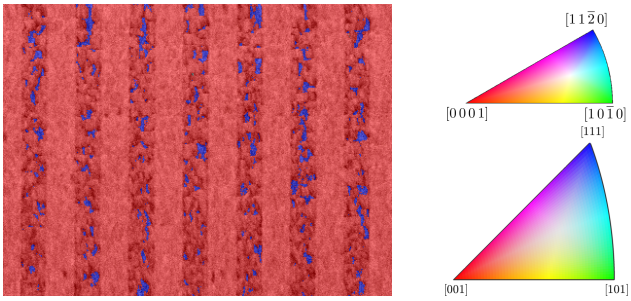

a) IPF-Z coloring (Laue group) + pattern quality

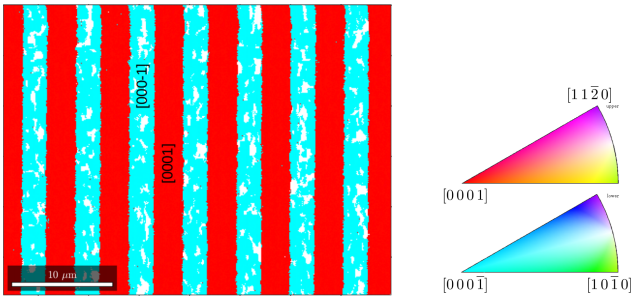

b) IPF-Z coloring using the MTEX-color key for $6mm$.

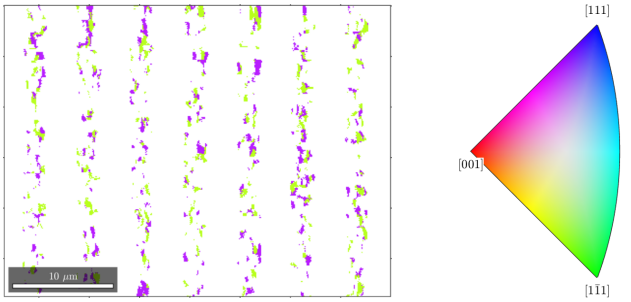

c) IPF-X coloring. The respective $\langle 1\,\bar{1}\,2\rangle$ and $\langle 1\,1\,2\rangle$ are defined by different colors in the MTEX-color key of $\bar{4}3m$.

Figure 17 Evidence of alternating $(0\,0\,0\,1)$- and $(0\,0\,0\,\bar{1})$-GaN epitaxially grown on a $(0\,0\,0\,1)$-oriented sapphire substrate. Whereas any Laue-group related color-key encoding of one of the standard directions X, Y or Z does neither show polarity nor existing twins (a), the application of the point-group related key does it (b+c) [53].

face ($(0\,0\,0\,1)$, red) and Ga-face ($(0\,0\,0\,\bar{1})$, light-blue) material can be distinguished. Please note that the applied MTEX-color key is virtually divided into two segments representing parts of the upper and the lower hemisphere. Along the arc both keys have exactly the same color so that they seamlessly match together [53].

The orientation data of the cubic GaN are separately displayed in Fig. 17 (c) since both modifications are of different symmetry and use separate color keys. The two appearing colors in (c) indicate the occurrence of twins. They are invisible in (a) because of the shared twinning plane perpendicular to the reference axis [0,0,1]. However, using the in (a) applied color key of $m\bar{3}m$ also the crystallographic encoding of [1,0,0] and [0,1,0] will not depict the twins because of the special alignment of the sample [53]: X $\|\langle 1\,1\,\bar{2}\rangle$, Y $\|\langle 1\,\bar{1}\,0\rangle$ and Z $\|\langle 1\,1\,1\rangle$. Therefore, for a visualization the color key of the point group is used in (c). A short inspection of the color key is sufficient to recognize that it contains two independent $[1\,\bar{1}\,2]$ (greenish) and $[1\,1\,2]$ (violett). In contrast, even for Y $\|\langle 1\,\bar{1}\,0\rangle$ this color key cannot differentiate between both twin orientations. Moreover, the polarity of the cubic GaN does not change and is the same as of the surrounding hexagonal GaN. Therefore, also the IPF map of Z$\|\langle 1\,\bar{1}\,1\rangle$ would be encoded uniformly in green and unable to display the existing twins by different colors.

Caused by the epitaxial growth of the hexagonal GaN on sapphire, BKD patterns of GaN only switch the polarity which is mainly visible at the single (0001) band. In order to validate the success rate of the pattern matching with respect to different crystal orientations a polycrystalline but not cubic phase needs to be analyzed.

Example: Polycrystalline material The investigated ZnO is applied for varistors (non-linear ceramic resistors) which are used to protect electric and electronic circuits against overvoltages. The crystal structure of ZnO is again of wurtzite type. The FSD image in Fig. 18 (a) displays a ceramic matrix with grains up to 10µm in diameter. The round shaped particles protruding from the matrix are cubic Bi_2O_3 which is one of the typical additives used. They are not further discussed and shown in the orientation maps as white areas.

Since the property of a varistor is assumed to change with the grain size, EBSD has been selected to characterize the microstructure. However, the orientation map in Fig. 18 (b) display several single grains which are indicated in (a) as two grains since they show clearly visible intergranular boundaries and an abrupt change in surface topography as well. On the other hand, the pattern quality map which is very sensitive to high-angle boundaries did not reflect a significant variation along the visible lines. This led to the conclusion that the visible lines are very likely traces of twinning planes $\|$ to $(0\,0\,0\,1)$. This twinning law does not change any band position. However, it changes the asymmetry character of polar lattice planes which should be detectable by pattern matching. The result is shown in Fig. 18 (c). Now all visible grains in (a) are also correctly identified and differently color-coded in (c). The inserted black lines additionally emphasize the traces of discovered twinning planes.

4.4 Space-group sensitivity Simulated and experimental BKD patterns have been also applied for the discrimination of crystals with different chirality. For the analyzed quartz higher resolved BKD patterns were required in order to be sensitive to the small intensity variations involved [59]. With the help of difference plots of simulations, the sensitive features in orientation-dependent BKD pattern can be identified. Especially in case of small inten-

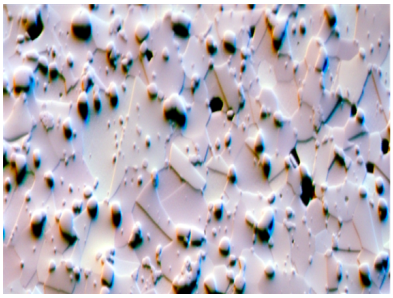

a) FSD image (ARGUS™)

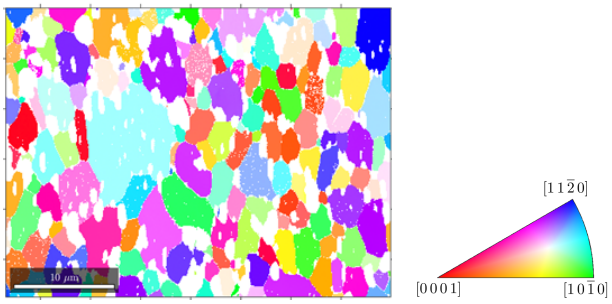

b) IPF coloring (Laue-group symmetry: 6/mmm)

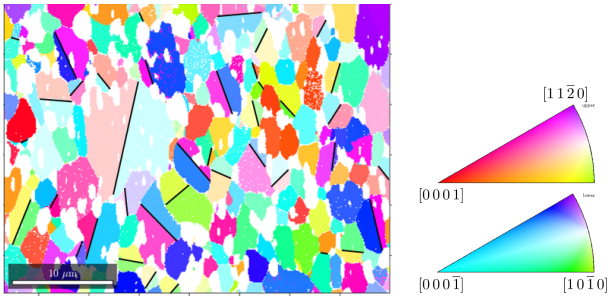

c) IPF coloring (point-group symmetry: 6mm)

Figure 18 Microstructure of ZnO. The white areas in (b) & (c) are occupied by Bi_2O_3. (b) shows the original orientation results for the centrosymmetric Laue group. The reanalyzed map (c) recognized the inversion twins by pattern matching and the polarity could be correctly extracted and differently encoded using a point-group specific color key in MTEX [53]. Some of the most prominent inversion twin boundaries are marked with black lines.

sity variations excess-deficiency effects may influence the analysis [60].

The possible chirality discrimination demonstrates that BKD patterns can be space-group selective by inherently carrying extensive crystal-structure information. This has also been utilized in a holographic approach to recover the crystal structure directly from BKD data [61], involving the examples of a simple body-centered cubic phase (W), as well as for the more complex pyrite structure.

5 Lattice parameter determination

The idea of using EBSD as tool for local phase identification in the SEM is as old as the technique itself. However, phase identification on precipitates which do not enable a successful identification (ID) by x-ray diffraction because of its low fraction is still a typical domain of transmission electron microscopy (TEM). Here EBSD was assumed to become a powerful and easy to handle alternative since despite comparable limitations to TEM, the used equipment, the operation as well as the sample preparation are much cheaper. Thus, already in 1996 GOEHNER and MICHAEL demonstrated the capabilities of EBSD for phase ID [62].

The procedures are not much different in TEM and SEM. A simple phase search based on EDX information is nowadays standard in most of the commercial EBSD software packages. One only needs a BKD pattern of suitable quality, a well-known projection-center position, and some time since all previously by EDX selected candidates have to be checked by their match with the experimental Kikuchi band positions. Some software packages also consider the approximate band widths but no software takes the band intensities into account.

Phase ID is in general impossible if the wanted phase is missing in the available databases. This might be related to a slightly different chemical composition, or the crystal structure has not yet been described. In such cases a reasonably reliable lattice parameter characterization would be very helpful to succeed. Unfortunately, caused by the short electron wavelength and the resulting small Bragg angles EBSD is assumed to be very inaccurate in lattice parameter determination. Latest investigations of DINGLEY and WRIGHT [63,64] confirmed again that even under best conditions accuracy and precision cannot become better than 5%. Thus, it was even more surprising that recently a software (EBSDL) has been presented which claimed to be able to reach a noticeably better accuracy and precision even under worse conditions [65].

We will present first results where EBSD helped to identify and describe unknown phases.

5.1 High-resolution BKD patterns

During production of superconducting magnets the following phases are expected: Nb_3Sn, Cu_6Sn_5, Cu_3Sn, Cu and Nb [66]. However, investigating high-energy synchrotron XRD experiments (ID15A beamline at ESRF, Grenoble) some minor peaks could not be assigned to one of these phases.

Accordingly, microstructure investigations of the same material by EBSD identified grains which delivered BKD patterns of sufficient quality, cf. Fig. 19 (b). But since the collected EDX signal and Kikuchi band positions did not match a phase in the available databases a phase assignment respectively indexing of the BKD patterns was impossible.

A simple inspection already indicates that due to missing symmetry elements the BKD pattern in Fig. 19 (b) is evidently incompatible with any cubic symmetry. However, at the bottom left corner a single three-fold or six-fold rotation symmetry appears which indicates a hexagonal or trigonal/rhombohedral Bravais lattice, or a respectively pseudosymmetric lattice of lower symmetry.

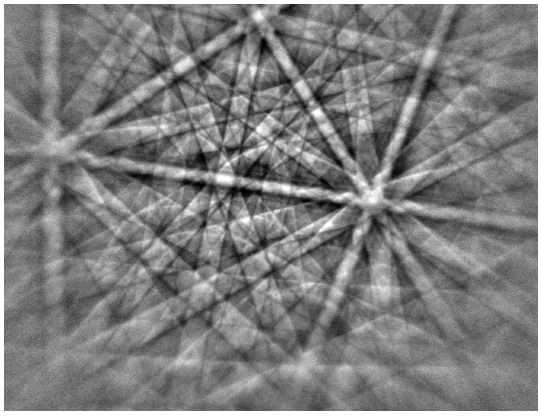

a) BKD pattern of Cu

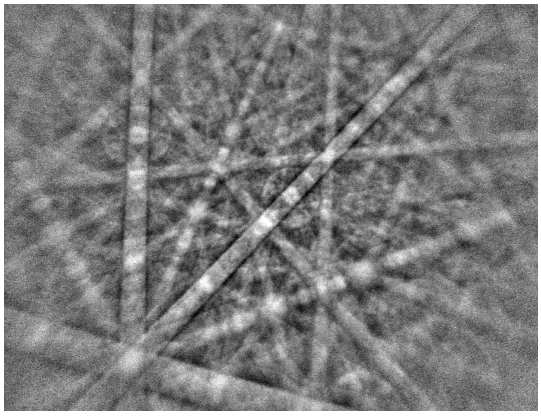

b) unknown phase

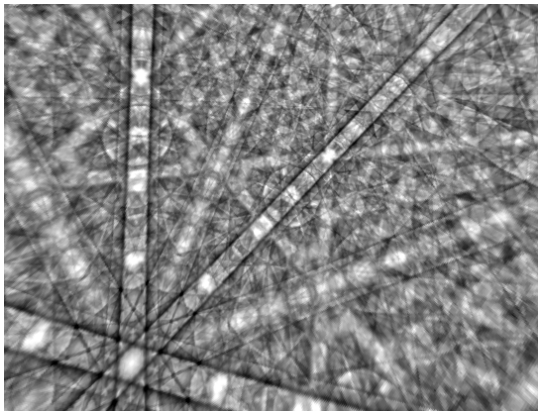

c) simulated pattern of $(Nb_{.75},Cu_{.25})Sn_2$

Figure 19 Bravais-lattice and lattice-parameter determination using a single BKD pattern of high resolution (b), (Nordlys, Oxford Instr.). For an optimal positioning of the projection center a Cu pattern (a) has been used. The derived lattice parameters have been used to identify and refine the phase by XRD. The BKD simulation is given in (c).

In order to extract both Bravais lattice as well as the respective lattice parameters, EBSDL has been applied to the non-binned BKD pattern[4]. A detailed description how EBSDL works is given in [65]. In short summary: The implemented algorithm requires a maximum number of as accurate as possible defined band positions and band widths.

For a perfect definition of the projection-center position a high-resolved BKD pattern collected on an adjacent Cu grain has been used, cf. Fig. 19 (a).

It is striking that compared to the Cu pattern many bands formed by the unknown phase (b) look much more diffuse. They can be considered by accurate positions but their widths can be only roughly estimated. Incidentally, the numerous narrow bands in (b) indicate a phase with clearly higher lattice parameters than Cu. Since the relative error is bigger for narrow than for wider bands, this all makes a determination of lattice parameters very difficult and challenging.

Despite these difficulties, the Bravais lattice has been proposed by EBSDL to be hexagonal. The derived lattice parameters are shown in Table 5 and compared with the lattice parameters later refined from the powder XRD data.

Table 5 Lattice parameter determination of an unknown phase using EBSDL [65] and Rietveld refinement of synchrotron XRD data using MAUD [67].

	a [Å]	c [Å]	c/a
EBSD	5.27	13.08	2.48
XRD	5.645(1)	14.124(5)	2.502
deviation	-6.9%	-7.7%	-0.8%

The comparatively low but not disappointing accuracy has mainly the following reasons:

1. numerous narrow and diffuse bands,
2. a systematic overestimation of the band widths by the operator (Is the Bragg position better described by the bright or the dark part of the band edge?), and
3. a possibly longer wavelength caused by charging on the surface and a reduction of the effective electron energy.

After multiple use of EBSDL it is noticeable that the derived lattice parameters tend to be smaller, cf. list item 2 and 3. However, the resulting lattice-parameter ratios are commonly better than $\pm 1\%$. This has been already pointed out in [63]. We believe that this has its reason in the fact that the lattice-parameter ratio only depends on the band positions which can be determined rather accurately. Much more problematic is an exact determination of a band width defining the absolute position of the Bragg angle.

Although the result is less accurate than generally expected, the Bravais-lattice type as well as the lattice parameters derived by EBSD were the key indication to focus on transition-metal distannides with hexagonal symmetry and similar lattice parameters. Based on this assumption

[4] 1343×1024 pixels, Nordlys detector, Oxford Instr.

the lattice parameters and the crystal structure data have been successfully refined [66].

In order to get an impression how good the simulated BKD pattern derived from the crystal structure description in [66] correlate with the experimental pattern, the simulation is displayed in Fig. 19 (c). Both pattern show a satisfying coincidence. The simulation does not take into account the anisotropic distribution of the backscattered signal, cf. Fig. 9. This is the reason why the experimental BKD pattern loses brilliance and becomes significantly more noisy with increasing gnomonic distortion. The larger the distance to the intensity maximum of the raw pattern, the smaller the signal-to-noise ratio.

It could be expected that a higher image resolution should always result in a higher precision of the extracted data like Kikuchi band widths and positions [68], and thus the resulting crystal orientations and lattice parameters. However, the example which we just discussed showed that a higher image resolution can be beneficial only when it is accompanied by a respective increase of resolvable "information density". Even if we could record the image in Fig. 19 (b) with a ten times higher image resolution we would not necessarily get a better result than listed in Table 5. The question is rather which image resolution would be appropriate to use EBSD for a meaningful determination of lattice parameters? How far can we get with BKD patterns in standard resolution?

5.2 Low-resolution BKD patterns It has been previously found that Co-based alloys like Co–Al–W undergo precipitation hardening of the γ matrix similar to Ni-based superalloys [69]. The solid solution of the non-ordered γ matrix (Co,Al) locally transforms to an ordered intermetallic-compound $Co_3(Al,W)$ called γ'.

After diffusion welding, numerous clusters of hexagonal Co_3W grains are formed, cf. Fig. 20. The Co_3W clusters are surrounded by a γ/γ' matrix, cf. the upper left corner where γ' (white) is coherently embedded in γ. Locally also cubic $\beta-$CoAl occurs. Most interesting is that Co_3W forms remarkable BKD patterns.

It was remarkable that despite a very good pattern quality the indexing of Co_3W fractionally failed for entire grain parts. A closer inspection of the BKD patterns showed that within suspicious grains the patterns only look similar. Surprisingly, a major part of the BKD patterns keeps absolutely unaffected but some narrow bands noticeably change their positions if one moves between adjacent measurement spots. This variation correlates with a lamellar substructure only rudimentarily visible in individual grains of Fig. 20. The aim is to analyze these varying BKD patterns by EBSDL and determine Bravais lattice as well as lattice parameters if possible.

For a manual selection of band positions and widths noise-poor and brilliant BKD patterns are preferred. Therefore, BKD patterns of a map need to be averaged. As appropriate selection criterion for suitable pattern the cross-correlation coefficient r can be applied again. Only patterns with a high correlation to a selected pattern will be considered. This allows a semi-automation of this task. In a first run and for a predefined area of an orientation map, r will be calculated for all patterns. In a second run only the patterns with the highest correlation will be averaged. The resulting averaged patterns are presented in Fig. 21 (a) and (b). They represent the end members of a number of continuously changing BKD patterns. In the following we will only refer to the end members (a) and (b).

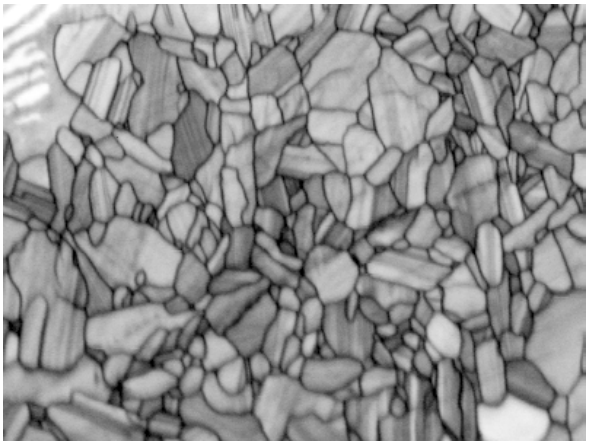

Figure 20 Imaging of the cross correlation coefficient of BKD (i.e. background-subtracted) patterns of adjacent map positions. Within the displayed clusters, the Co_3W grains show an inherent lamellar substructure.
(map size:400×300 pixels, step size: 56nm)

In both patterns the bands with obviously different positions are marked by red-dotted lines. The BKD pattern in (c) indicates the signal part which is invariant in (a) and (b). It represents a superimposition of about 20 patterns collected at adjacent measurement positions in a single grain. By pattern averaging the variable part of the patterns annihilates and only the constant part remains. It displays some kind of supergroup symmetry which fits to the point-group symmetry of Co_3W. It is described by $6/m\,mm$, i.e., $\perp\, c$ every each 30° a mirror plane occurs. The mirror planes are sketched in (c) by black lines intersecting in $[0\,0\,0\,1]$.

In contrast, mainly because of red-marked bands the BKD pattern in (b) does not reflect this high symmetry. The half of all mirror planes vanish so that in maximum a three-fold symmetry remains. Since the search within the available crystal-structure databases did not find any matching candidate for a Co–Al–W containing phases a lattice-parameter determination hopefully helps to restrain the search parameters.

Using the available patterns in Fig. 21 (a) we derived by EBSDL lattice dimensions for Co_3W with a satisfying agreement, cf. Table 6.

For the BKD patter of the unknown phase in (b) we determined lattice parameters of $a_o = 5.06$Å and $c_o = 18.29$Å. A new database search discovered a hit

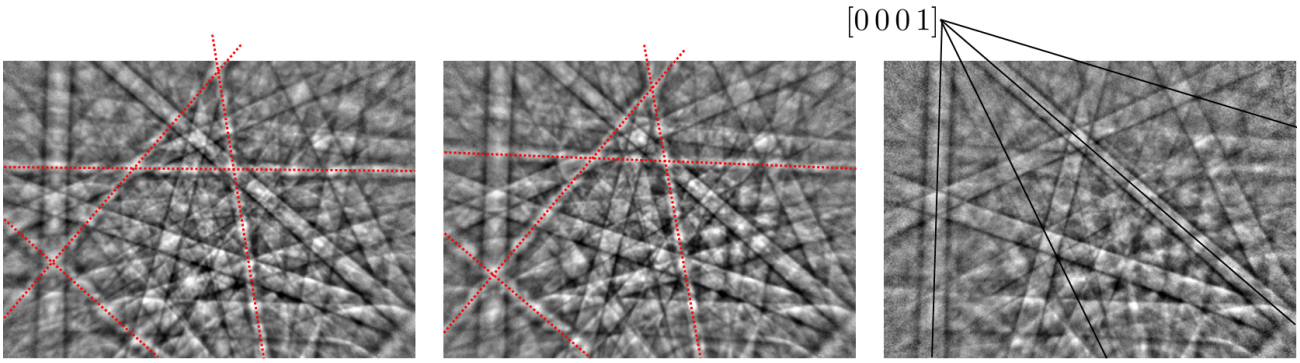

a) Co_3W (hexagonal) b) Co_3Ta (rhombohedral) c) "invariant" signal

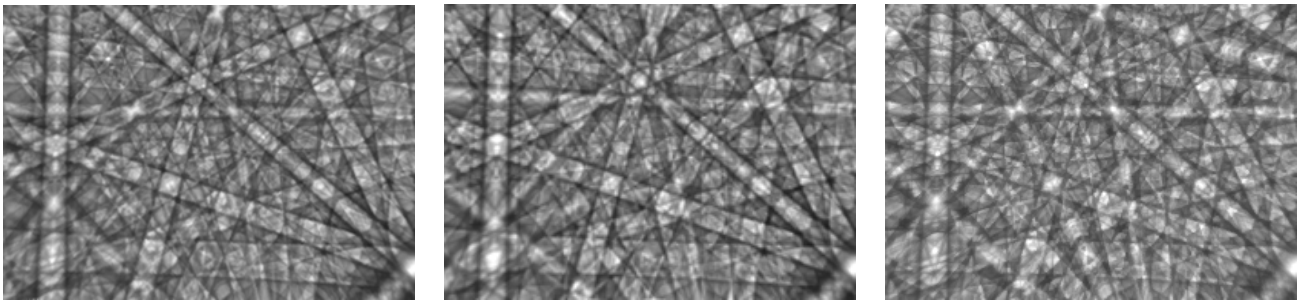

d) simulation ABABCBCB... e) simulation ABABCBCBC... f) simulation AB...

Figure 21 Averaged pattern of Co–W–Ta phases. The pattern resolution is 160×115 pixels only. (a) matches to a grain with hexagonal stacking, and (b) to a grain with a rhombohedral stacking. (c) reflects the "invariant" part of (a) and (b). It considers all patterns where the stacking apparently continuously changes so that during averaging all variant parts of the images disappear.

Table 6 Comparison of lattice parameters listed in ICSD (Inorganic Crystal Structure Database) for the close-packed structures of Co_3W and Co_3Ta, and derived by EBSDL from the BKD patterns (160×115 pixels) shown in Fig. 21.

		Co_3W	$\beta-Co_3Ta$
ICSD	a_o [Å]	5.120	5.186
	c_o [Å]	4.120	18.870
	c_o/a_o	0.804	3.639
EBSDL	lattice	hexagonal	rhombohedral
	a_o [Å]	5.02 (-4%)	5.06 (-5%)
	c_o [Å]	4.03 (-4%)	18.29 (-6%)
	c_o/a_o	0.803 (-.2%)	3.615 (-1%)

for $\beta-Co_3Ta$ which immediately indexed the majority of the missing BKD patterns. However, EDX maps clearly showed that this phase does not occur it this composition so that we assume a phase Co_3(Al,W,Ta) with the same or a similar structure type.

5.3 Polytypes Comparing all crystal structures it is striking that except of $\beta-$CoAl the identified structures are based on a dense stacking of close-packed and well-ordered Co_3X layers (X=Al, W, Ta).

Only the different stacking sequence of in first approximation identical Co_3X layers decides about the final symmetry of the resulting structure [70,71]. An even stacking sequence like AB..., ABAC... or ABABCB... is often of hexagonal symmetry whereas an odd stacking sequence like ABCAC... or ABCBABC... results in a rhombohedral or hexagonal symmetry group. A special case is the well-known sequence ABC... which can even form a cubic symmetry as for γ' or γ, see Fig. 22. Accordingly, the thickness of a single layer in all structures is quite constant:

$1/2c_o$ = 2.01Å (Co_3W, hexagonal)
$1/9c_o$ = 2.10Å ($\beta-Co_3Ta$, trigonal)
$1/3\sqrt{3}\,a_o$ = 1.94Å (γ', cubic).

A comparison of the experimental pattern with simulations of different polytypes showed that the cross-correlation coefficient even increases if for the unknown phase another stacking sequence is selected. Instead of ABABCBCAC... a stacking ABABCBCBC... matches even better. However, also for the assumed hexagonal phase with stacking AB... – Fig. 21 (d) – a hypothetical polytype ABABCBCB... (f) matches the experimental intensity distribution in (a) also slightly better.

The pattern in (f) is derived from a unit cell which is along c four times longer compared to (d). Surprisingly, this does not remarkably affect the patterns by a formation of more narrow bands. It also underlines that for polytypes this simple correlation does not work. In case of a sim-

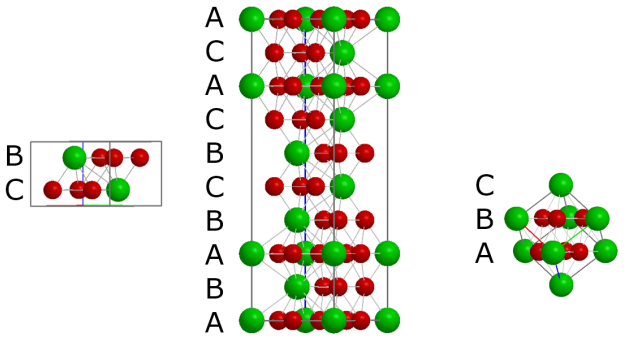

Figure 22 Different stacking of the "same" layer ends up in different phases. Please note that the discovered phase is describable by comparable lattice parameters as $\beta-Co_3Ta$ but by a different stacking sequence.

ple pseudosymmetry of the crystal lattice the derived basis vectors are perhaps a multiple or a rational fraction of the real value. As for other standard diffraction techniques pseudosymmetry is a limiting factor.

Nevertheless, the example demonstrated that the application of low-resolved patterns for lattice parameter determination is not doomed to failure from the beginning. On the other hand, the manually extractable information of a BKD pattern does not scale automatically with the applied image resolution.

6 Summary

6.1 Use of the background signal The raw EBSD signal offers additional information compared to only the BKD part which is used in standard orientation analyses. The raw EBSD signal carries information about the mean atomic number ($\bar{Z}$) for phase separation. Despite the missing energy resolution, this can be beneficial when EDX is not able to collect a sufficiently discriminating signal in the short acquisition time, or the information volumes of EBSD and EDX are too different (higher magnification, high acceleration voltage). Despite the new EDX detectors, the dwell time for EBSD can be often too short for a reliable EDX investigation.

Relative to a hardware BSE detector, the dwell time selected for EBSD-pattern acquisition is extremely long, and thus the signal-to-noise ratio of EBSD-derived BSE images is usually much better than in BSE hardware images. This can improve the phase discrimination capabilities of EBSD. Disturbing effects are surface topography and orientation related signals if they become more pronounced than $\Delta\bar{Z}$ of the investigated phases.

The use of $\Delta\eta \propto \Delta\bar{Z}$ offers an opportunity which may be helpful for phase confirmation and discrimination. Very beneficial is that neither specific equipment nor additional time is necessary.

The most relevant impact of using the raw EBSD signal is that it is sure that all the extracted signals for a map point were collected at the same time, with the same duration and from the same measurement point. In contrast to images acquired before or after an EBSD mapping using a BSE detector, from raw EBSD pattern derived BSE images exactly fit to the orientation information derived from the BKD patterns.

Moreover, it has been shown that the background signal also mainly contributes to the orientation contrast imaging since the major component of this signal is caused by the channeling-in of electrons and not by the BKD pattern. Although very sensitive an orientation or misorientation quantification is impossible. The application of COI (center of intensity), however, enables a semi-quantitative evaluation of misorientation in high precision but it needs the orientation and is strongly affected by the other parameters, i.e., surface topography and $\bar{Z}$.

6.2 Overcoming current restrictions Even standard EBSD patterns allow a clearly improved orientation precision compared to the current standard procedures, which is seen by the improvement supplied by pattern matching approaches.

Consequent implementation of point-group sensitive EBSD could solve important general problems like the determination of the polarity of planes or directions.

The proposed reprocessing of an orientation mapping of cubic materials like GaP [55] or pyrite [52] is comparatively simple. However, investigation of GaN and ZnO confirmed that the applied procedure also works for non-cubic as well as multiple-phase materials [72]. However, the method is clearly limited to elements that exhibit a sufficient difference in the scattering strengths for electrons, which excludes compounds such as GaAs, for example [73].

Also, the limitations of lattice parameter determination by EBSD is not simply a matter of pattern resolution but includes limitations of band positions and widths, and uncertainties regarding the energy of the diffracting electrons. Nevertheless, Bravais lattice and lattice parameters of unknown phases have been determined either by a single high-resolved pattern only or by high-binned BKD patterns. Although in both cases the conditions were far away from being perfect the derived results delivered useful starting information for a further crystal structure refinement, and for a first understanding of the formation of polytypes in Co–Al–W alloys.

Acknowledgements We would like to express our special thanks to P. Gille (LMU Munich, Germany) for the kindly appropriation of the quasicrystal (Fig. 1), T. Schlothauer (TU Freiberg, Germany) for the mineralogical sample used in Fig. 4, A. Epishin (TU Berlin, Germany) for the CMSX4 sample in Fig. 5 and the Co-Al sample in Fig. 20, A. Kranzmann (BAM Berlin, Germany) for the corrosion sample used in Fig. 6, J. Götze (TU Freiberg,

Germany) for the quartz sample characterized in Fig. 7, 10 and 13, A.P. Boyle (Uni Liverpool, UK) for the framboidal pyrite shown in Fig. 14 and 15, V. Lebedev (FhI for Applied Solid State Physics, Freiburg, Germany) and M. Himmerlich (TU Ilmenau) for the GaN heterostructure characterized in Fig. 17, A. Reichmann (TU Graz) for the ZnO sample investigated in Fig. 18, and S. Martin (TU Freiberg) for the BKD pattern used for the lattice parameter determination (Fig. 19). Moreover, we thank M. Han and L. Li (East China Jiaotong University, Nanchang) for the deployment of *EBSDL*, a software for lattice parameter determination from single BKD patterns. We gratefully thank Michaela Buchheim and Romeo Saliwan-Neumann for the successful preparation of numerous samples and countless EBSD and EDX measurements. M. Kay is acknowledged for correcting the manuscript.

References

[1] D. Naumović, P. Aebi, L. Schlapbach, C. Beeli, K. Kunze, T. A. Lograsso, and D. W. Delaney, Phys. Rev. Lett. **87**(19), 195506 (2001).
[2] A. Winkelmann, Electron Backscatter Diffraction in Materials Science, (Springer Science+Business Media, 2009), chap. 2. Dynamical Simulation of Electron Backscatter Diffraction Patterns., pp. 21–33.
[3] R. C. Gonzalez and R. E. Woods, Digital Image Processing., 3rd edition (Prentice Hall, Upper Saddle River, New Jersey, 2002).
[4] X. Tao and A. Eades, Microsc. Microanal. **11**(4), 341–53 (2005).
[5] A. Winkelmann, Ultramicroscopy **108**, 1546–1550 (2008).
[6] H. Niedrig, Scanning **1**(1), 17–34 (1978).
[7] O. C. Wells, Scanning **2**(4), 199–216 (1979).
[8] E. I. Rau and L. Reimer, Scanning **23**(4), 235–240 (2001).
[9] L. Reimer, Scanning Electron Microscopy: Physics of Image Formation and Microanalysis, 2nd edition (Springer-Verlag, Berlin Heidelberg New York, 1998).
[10] D. J. Prior, P. W. Trimby, U. D. Weber, and D. J. Dingley, Mineral. Mag. **60**(6), 859–869 (1996).
[11] A. P. Day and T. E. Quested, J. Microscopy **195**(3), 186–196 (1999).
[12] S. I. Wright and M. M. Nowell, Microsc. Microanal. **12**(01), 72–84 (2006).
[13] R. A. Schwarzer and J. Sukkau, Banaras Metall **18**, 1–11 (2013).
[14] S. I. Wright, M. M. Nowell, R. de Kloe, P. Camus, and T. Rampton, Ultramicroscopy **148**(1), 132–145 (2015).
[15] D. Berger and H. Niedrig, Scanning **21**(3), 187–190 (1999).
[16] R. A. Schwarzer, J. Sukkau, and J. Hjelen, Imaging of topography and phase distribution with an EBSD detector in the SEM, in: Microscopy Conference, Kiel, Germany, (2011).
[17] A. Winkelmann and M. Vos, Ultramicroscopy **125**(2), 66–71 (2013).
[18] O. C. Wells, L. M. Gignac, C. E. Murray, A. Frye, and J. Bruley, Scanning **28**(1), 27–31 (2006).
[19] E. Payton and G. Nolze, Microsc. Microanal. **19**(4), 929–941 (2013).
[20] R. Schwarzer and J. Sukkau, Prakt. Metallogr. (Sonderband) **45**, 227–232 (2013).
[21] R. A. Schwarzer and J. Hjelen, Microscopy Today **23**(1), 12–17 (2015).
[22] G. E. Lloyd, Mineral.Mag. **51**, 3–19 (1987).
[23] P. G. Howell, K. M. W. Davy, and A. Boyde, Scanning **20**(1), 35–40 (1998).
[24] D. P. Harding, Miner. Metallurg. Process. **19**(4), 215–219 (2002).
[25] J. I. Goldstein, D. E. Newbury, P. Echlin, D. C. Joy, A. D. Romig, C. E. Lyman, C. Fiori, and E. Lifshin (eds.), Scanning Electron Microscopy and X-Ray Microanalysis., 2nd edition (Plenum Press, New York and London, 1992).
[26] S. J. B. Reed, Electron microprobe analysis and scanning electron microscopy in geology, 2nd edition (Cambridge University Press, New York, 2005).
[27] D. H. Krinsley, K. Pye, S. Boggs, and N. K. Tovey, Backscattered Scanning Electron Microscopy and Image Analysis of Sediments and Sedimentary Rocks. (Cambridge University Press, 1998).
[28] A. Dubus, Microsc. Microanal. Microstruct. **2**, 475–481 (1991).
[29] F. Zupanič, Mater. Charact. **61**(12), 1335–1341 (2010).
[30] F. Zupanič, T. Bončina, and B. Markoli, Use of electron backscattering coefficients for identification of Be-bearing phases, in: Microscopy: Science, Technology, Applications and Education, edited by A. Méndez-Vilas and J. Díaz, , Microscopy Series Vol. 3 (FORMATEX, Badajoz, Spain, 2010), pp. 1824–1829.
[31] A. J. Schwartz, M. Kumar, B. L. Adams, and D. P. Field (eds.), Electron Backscatter Diffraction in Materials Science (Springer Science+Business Media, 2009).
[32] C. Schulze and M. Feller-Kniepmeier, Mater. Sci. Engin. **A281**, 2004–212 (2000).
[33] G. Nolze and A. Winkelmann, Cryst. Res. Technol. **49**(7), 490501 (2014).
[34] G. Nolze, A. Winkelmann, R. Hielscher, and E. Payton, EBSD: more reliable and precise, EBSD Workshop: Applications in Material and Earth Science, Belo Horizonte (Brazil), 17.+18.09. 2015.
[35] S. Zaefferer and N. N. Elhami, Acta Mater. **75**, 20–50 (2014).
[36] H. Mansour, J. Guyon, M. A. Crimp, N. Gey, B. Beausir, and M. Maloufi, Scripta Mater. **84-85**, 11–14 (2014).
[37] A. Weidner and H. Biermann, Phil. Mag. **95**(7), 795–793 (2015).
[38] T. Ichinokawa, M. Nishimura, and H. Wada, J. Phys. Soc. Jap. **36**(1), 221–226 (1974).
[39] M. Chapman, P. Callahan, and M. DeGraef, Scripta Mater. **120**, 23–26 (2016).
[40] F. J. Humphreys, Y. Huang, I. Brough, and C. Harris, J. Microscopy **195**(3), 212–216 (1999).
[41] E. F. Rauch, M. Vron, J. Portillo, D. Bultreys, Y. Maniette, and S. Nicolopoulos, Microsc. Analys. **22**(6), S5–S8 (2008).
[42] P. G. Callahan and M. De Graef, Microsc. Microanal. **19**(June), 1255–1265 (2013).
[43] Y. H. Chen, S. U. Park, D. Wei, G. Newstadt, M. J. J. P. Simmons, M. DeGraef, and A. O. Hero, Microsc. Microanal. **21**, 739–752 (2015).
[44] S. I. Wright, M. M. Nowell, S. P. Lindeman, P. P. Camus, M. De Graef, and M. A. Jackson, Ultramicroscopy **159**(Dec), 8194 (2015).

[45] A. J. Wilkinson, G. Meaden, and D. J. Dingley, Ultramicroscopy **106**(4-5), 307–13 (2006).
[46] T. B. Britton, C. Maurice, R. Fortunier, J. H. Driver, A. P. Day, G. Meaden, D. J. Dingley, K. Mingard, and A. J. Wilkinson, Ultramicroscopy **110**(12), 1443–53 (2010).
[47] K. Mingard, A. Day, C. Maurice, and P. Quested, Ultramicroscopy **111**(5), 320–9 (2011).
[48] S. I. Wright, M. M. Nowell, and D. P. Field, Microsc. Microanal. **17**(3), 316–29 (2011).
[49] C. Maurice, J. H. Driver, and R. Fortunier, Ultramicroscopy **113**(Feb), 171–181 (2012).
[50] A. J. Wilkinson and T. B. Britton, Materials Today **15**(9), 366 – 376 (2012).
[51] S. I. Wright, M. M. Nowell, R. de Kloe, and L. Chan, Microsc Microanal **20**(03), 852–863 (2014).
[52] G. Nolze, A. Winkelmann, and A. P. Boyle, Ultramicroscopy **160**(1), 146–154 (2016).
[53] G. Nolze and R. Hielscher, J. Appl. Cryst. **49**, 1786–1802 (2016).
[54] K. Z. Baba-Kishi and D. J. Dingley, Scanning **11**, 305–312 (1989).
[55] A. Winkelmann and G. Nolze, Appl. Phys. Lett. **106**, 072101 (2015).
[56] G. Nolze, V. Geist, G. Wagner, P. Paufler, and K. Jurkschat, Z. Kristal. **193**(1-2), 111–126 (1990).
[57] G. Nolze, Einsatz der Interferenzen aus Gitterquellen (Kossel-Effekt) zur Charakterisierung von $A^{III}B^{V}$-Verbindungen mit Zinkblendestruktur., PhD thesis, Universität Leipzig, Fakultät f. Mathem. Naturwissensch., 1991.
[58] M. Stutzmann, O. Ambacher, M. Eickhoff, U. Karrer, A. L. Pimenta, R. Neuberger, J. Schalwig, R. Dimitrov, P. J. Schuck, and R. D. Grober, phys. stat. sol. (b) **228**, 505–512 (2001).
[59] A. Winkelmann and G. Nolze, Ultramicroscopy **149**(2), 58–63 (2015).
[60] A. Winkelmann, Ultramicroscopy **108**(12), 1546–1550 (2008).
[61] T. Lühr, A. Winkelmann, G. Nolze, D. Krull, and C. Westphal, Nano Lett. **16**(5), 3195–3201 (2016).
[62] R. P. Goehner and J. R. Michael, J. Res. Natl. Inst. Stand. Technol. **101**(3), 301–308 (1996).
[63] D. J. Dingley and S. I. Wright, J. Appl. Cryst. **42**(2), 234–241 (2009).
[64] D. J. Dingley and S. I. Wright, Electron Backscatter Diffraction in Materials Science., 2nd edition, (Springer Science + Business Media, 2009), chap. 7. Phase Identification Through Symmetry Determination in EBSD Patterns., pp. 97–107.
[65] L. Li and M. Han, J. Appl. Cryst. **48**(1), 107–115 (2015).
[66] S. Martin, A. Walnsch, G. Nolze, A. Leineweber, F. Leaux, and C. Scheuerlein, Intermetallics, (in press) (2016).
[67] L. Lutterotti, S. Matthies, and H. R. Wenk, Newsletter CPD **21**, 14–15 (1999).
[68] F. Ram, S. Zaefferer, and D. Raabe, J. Appl. Cryst. **47**(1), 264–275 (2014).
[69] J. Sato, T. Omori, K. Oikawa, I. Ohnuma, R. Kainuma, and K. Ishida, Science **312**, 90–91 (2006).
[70] D. Pandey and P. Krishna, International Tables for Crystallography, (Kluver Academic Publishers, Doordrecht – Boston – London, 1992), chap. 9.2.1 Layer stacking in close-packed structures, pp. 660–667.
[71] E. Prince (ed.), International Tables for Crystallography: Volume C. Mathematical, Physical and Chemical Tables., 3rd edition (Kluver Academic Publishers, Doordrecht – Boston – London, 2004).
[72] A. Winkelmann, G. Nolze, M. Himmerlich, and A. Reichmann, Point group sensitive orientation mapping using EBSD, in: 6th Int. Conf. Recryst. Grain Growth, Pittsburg, PA, USA, (2016).
[73] G. Nolze, C. Grosse, and A. Winkelmann, J. Appl. Cryst. **48**, 1405–1419 (2015).